

The deep-DRT: A Deep Neural Network Approach to Deconvolve the Distribution of Relaxation Times from Multidimensional Electrochemical Impedance Spectroscopy Data

Emanuele Quattrocchi^{a†}, Ting Hei Wan^{a†}, Alessio Belotti^a, Dohyung Kim^c, Simona Pepe^a,
Sergei V. Kalinin^d, Mahshid Ahmadi^c, and Francesco Ciucci^{a,b*}

^a Department of Mechanical and Aerospace Engineering, The Hong Kong University of Science and Technology, Hong Kong, China

^b Department of Chemical and Biological Engineering, The Hong Kong University of Science and Technology, Hong Kong, China

^c Joint Institute for Advanced Materials, Department of Materials Science and Engineering, University of Tennessee, Knoxville, TN 37996, USA

^d The Center for Nanophase Materials Sciences, Oak Ridge National Laboratory, Oak Ridge, TN 37831, USA

[†] Equally contributing authors

*Corresponding author: francesco.ciucci@ust.hk

Phone: +852 2358 7187

Fax: +852 2358 1543

Abstract

Electrochemical impedance spectroscopy (EIS) is an experimental technique ubiquitously used to study electrochemical systems. However, conventional EIS data interpretation through physical and equivalent circuit models is challenging because physical models are problem-specific, and equivalent circuits are often just lumped-element analogs lacking physical meaning. The distribution of relaxation times (DRT) has emerged as a complementary approach to resolve these issues. One drawback of conventional DRT deconvolution is that the EIS data is understood to be (only) a function of frequency (*i.e.* 1D data) and deconvolved accordingly. This work proposes a novel deconvolution method based on deep neural networks (DNNs), allowing the analysis of multidimensional EIS spectra to bridge data dependency on both frequencies and experimental conditions. Two particularly appealing traits of the deep-DRT method developed in this article are that neither regularization nor specific spacing on the state variables defining the experiment are required. Leveraging DNN to examine complex EIS spectra and their dependence on experimental conditions, this work opens a new research direction in the area of EIS analysis and DRT deconvolution.

Keywords:

- Electrochemical Impedance Spectroscopy
- Experimental-dependent DRT
- Deep learning
- Batteries
- Fuel and Solar cells

1 Introduction

Electrochemical impedance spectroscopy (EIS) [1] is one of the foundational methods in electrochemistry [2-4] and is used to gain physical and chemical insights across a broad range of timescales [5-7]. Despite its power, the interpretation of EIS data is challenging [8-10]. Conventional EIS interpretation methods are models based on lumped equivalent circuits [11, 12], or, in rare instances, physical models. Physical models are problem-specific and, in some cases, are characterized by a high computational cost [13]. Conversely, equivalent circuit models (ECMs) are just analogs, which often lack direct physical meaning [14-16], necessitating interpretation of the lumped circuit elements. Moreover, ECMs can be non-unique as EIS data may be modeled equally well by several circuits [16-19].

The distribution of relaxation times (DRT) is an alternative approach that can overcome the aforementioned issues of physical models and ECMs [20-23]. The DRT does not require equivalent circuits [24, 25] because it assumes that the EIS model $Z_{\text{DRT}}(f)$ is obtained from the following model [26, 27]:

$$Z_{\text{DRT}}(f) = i2\pi f L_0 + R_\infty + \int_{-\infty}^{\infty} \frac{\gamma(\log \tau)}{1 + i2\pi f \tau} d\log \tau \quad (1)$$

where f , τ , L_0 , and R_∞ are the frequency, timescale, inductance, and ohmic resistance, respectively, and $\gamma(\log \tau)$ is a distribution of timescales (or DRT). The main challenge associated with the DRT methodology is that regressing an experimental EIS spectrum against (1) is an ill-posed problem [28-30], in which the determination of $\gamma(\log \tau)$ depends strongly on experimental errors. Several approaches have been proposed to resolve this challenge [31], including ridge regression (RR) and elastic net [32-34], Monte Carlo methods [35, 36], genetic programming [37-39], maximum-entropy-based frameworks [40, 41], and Fourier transformations [42, 43].

Starting from RR [26, 27], our group reframed the DRT deconvolution as a Bayesian inverse problem allowing the penalty parameter and regression weights to be adjusted automatically as a function of $\log \tau$ [24, 44, 45]. Our team also showed that the DRT deconvolution can be obtained using machine learning techniques, including Gaussian processes [45] and (over-parametrized) deep-prior neural networks [46].

In its simplest form, the RR-based deconvolution of (1) requires minimizing the following loss function $\mathcal{L}(\boldsymbol{\gamma}, \lambda)$:

$$\mathcal{L}(\boldsymbol{\gamma}, \lambda) = \sum_{m=1}^M |Z_{\text{exp}}(f_m) - Z_{\text{DRT}}(f_m, \boldsymbol{\gamma})|^2 + \lambda P(\boldsymbol{\gamma}) \quad (2)$$

where $Z_{\text{exp}}(f_m)$ is the experimental EIS spectrum measured at frequencies f_m with $m = 1, 2, \dots, M$, $\boldsymbol{\gamma}$ is the vector of $\gamma(\log \tau)$ at specific collocation points (*i.e.* $\boldsymbol{\gamma} = [\gamma(\log \tau_1), \gamma(\log \tau_2), \dots, \gamma(\log \tau_N)]^\top$ with $\tau_1 < \tau_2 < \dots < \tau_N$), and $Z_{\text{DRT}}(f_m, \boldsymbol{\gamma})$ is the impedance obtained by discretizing $\gamma(\log \tau)$ in (1) through $\boldsymbol{\gamma}$ [26, 27]. Finally, $P(\boldsymbol{\gamma})$ is a penalty on $\boldsymbol{\gamma}$ weighted by a positive scalar λ [26] that is used to prevent overfitting.

While EIS spectra are collected at specific experimental conditions, they are typically deconvolved only relative to frequency. This limitation can be relaxed by taking EIS spectra to depend on some “experimental state.” For example, in the solid oxide fuel cell (SOFC) field, EIS spectra are often measured as a function of temperature, T , and oxygen partial pressure, p_{O_2} implying that we can rewrite the experimental impedance $Z_{\text{exp}}(f)$ in (2) as $Z_{\text{exp}}(f, T, p_{\text{O}_2})$ [47-49]. Incidentally, the abovementioned limitation goes well beyond EIS. In fact, the vast majority of (hyper) spectral datasets are analyzed one spectrum at a time without invoking proximity or correlations in parameter space (*e.g.* image plane, concentrations, etc.). Generally, if we define a set of (non-frequency) state variables $\boldsymbol{\psi}$ (for the fuel cell example $\boldsymbol{\psi} = [T, p_{\text{O}_2}]^\top$)

to represent the experimental conditions, we can replace the $Z_{\text{exp}}(f)$ in (2) with $Z_{\text{exp}}(f, \boldsymbol{\psi})$ [50] and write the DRT as $\gamma(\log \tau, \boldsymbol{\psi})$. Hence, while in its simplest formulation the DRT model, $Z_{\text{DRT}}(f)$, introduced by (1) can also be extended beyond the single frequency dimension to experimental conditions, leading to a broader multidimensional setting as $Z_{\text{DRT}}(f, \boldsymbol{\psi})$.¹ Throughout this article, we will leverage this notational insight by using neural networks as schematically presented in Figure 1. With reference to the notation just illustrated, the deep-DRT framework assumes that both the DRT, $\gamma(\log \tau, \boldsymbol{\psi})$, and the circuit parameters $[R_{\infty}(\boldsymbol{\psi}), L_0(\boldsymbol{\psi})]$ are deep neural networks (DNNs). The two DNNs are then optimized to minimize (2). More details will be provided in Section 2.3.

The advantages of the deep-DRT over conventional approaches are multifold. First, in contrast to other methods developed in the literature [50], no specific spacing/gridding on $\boldsymbol{\psi}$ is required. Second, the penalty term is not needed (*i.e.* λ in (2) can be set to zero). Third, the model is not only regressive, but can be framed to allow the prediction of $R_{\infty}(\boldsymbol{\psi})$, $L_0(\boldsymbol{\psi})$, and $\gamma(\log \tau, \boldsymbol{\psi})$ at untested experimental conditions.

The deep-DRT framework was validated using both artificial and real experimental data. Artificial EIS data allowed us to validate its consistency. In fact, the deep-DRT model could successfully predict $R_{\infty}(\boldsymbol{\psi})$, $L_0(\boldsymbol{\psi})$, and $\gamma(\log \tau, \boldsymbol{\psi})$ even when $\gamma(\log \tau, \boldsymbol{\psi})$ had overlapping or discontinuous features, and the $\boldsymbol{\psi}$ were selected randomly. Experimental datasets from a symmetric cell with a solid oxide cathode and a perovskite solar cell were then analyzed by the

¹ We assume that the measurement of $\boldsymbol{\psi}$ is history-independent, *i.e.*, the order of experiments does not affect the measurement.

deep-DRT method. The regression results compared closely to ECM models [51, 52] and, in addition to that, allowed for successful prediction.

The deep-DRT method developed herein mates in a multidimensional fashion DRT-based deconvolution of EIS data depending on experimental conditions. In this regard, this work opens a new stream of research that develops the study of regression and prediction of EIS data by exploiting DNN deconvolution coherently with experimental settings. Further, the deep-DRT methodology can be extended to other (hyper) spectral datasets.

2 Theory

The EIS spectra are usually measured as a function of experimental conditions. For example, as already outlined in the introduction, it is common to test the EIS of a SOFC for several combinations of T and p_{O_2} [53]. If these state variables are written as a vector $\boldsymbol{\psi} = [\psi_1, \psi_2, \dots, \psi_P]^\top$, then we can express the experimental impedance as a $(P+1)$ -dimensional function, $Z_{\text{exp}}(f, \boldsymbol{\psi})$. The first key idea of this article is to leverage the notation just introduced to use $R_\infty = R_\infty(\boldsymbol{\psi})$, $L_0 = L_0(\boldsymbol{\psi})$, and $\gamma(\log \tau) = \gamma(\log \tau, \boldsymbol{\psi})$ in (1). The second key idea is to encode the functions $R_\infty(\boldsymbol{\psi})$, $L_0(\boldsymbol{\psi})$, and $\gamma(\log \tau, \boldsymbol{\psi})$ in DNNs, which are trained based on an experimental dataset $S_\psi = \{\boldsymbol{\psi}_1, \boldsymbol{\psi}_2, \dots, \boldsymbol{\psi}_K\}$, where a specific experiment is characterized by a state $\boldsymbol{\psi} \in S_\psi$. The third key idea is to constrain the DNNs to comply with a discretized version of (1).

2.1 DRT Approximation of the Impedance

To solve (1) numerically, the DRT is taken at the collocation points $\log \boldsymbol{\tau} = [\log \tau_1, \log \tau_2, \dots, \log \tau_N]^\top$ [26, 27, 44]. Further, given the experimental state $\boldsymbol{\psi} \in S_\psi$, we

define $\boldsymbol{\gamma}(\log \boldsymbol{\tau}, \boldsymbol{\psi}) = [\gamma(\log \tau_1, \boldsymbol{\psi}), \gamma(\log \tau_2, \boldsymbol{\psi}), \dots, \gamma(\log \tau_N, \boldsymbol{\psi})]^\top$. It follows that (1) can be discretized as [26, 27]

$$\mathbf{Z}_{\text{DRT}}(\mathbf{f}, \boldsymbol{\psi}) = i2\pi L_0(\boldsymbol{\psi})\mathbf{f} + R_\infty(\boldsymbol{\psi})\mathbf{1} + \mathbf{A} \boldsymbol{\gamma}(\log \boldsymbol{\tau}, \boldsymbol{\psi}) \quad (3)$$

where $\mathbf{Z}_{\text{DRT}}(\mathbf{f}, \boldsymbol{\psi}) = [Z_{\text{DRT}}(f_1, \boldsymbol{\psi}), Z_{\text{DRT}}(f_2, \boldsymbol{\psi}), \dots, Z_{\text{DRT}}(f_M, \boldsymbol{\psi})]^\top$ is the vector of impedances of the DRT-model, computed at $\mathbf{f} = [f_1, f_2, \dots, f_M]^\top$ and $\boldsymbol{\psi}; \mathbf{1} = [1, 1, \dots, 1]^\top \in \mathbb{R}^M$; and $\mathbf{A} = \mathbf{A}_{\text{re}} + i\mathbf{A}_{\text{im}}$, with \mathbf{A}_{re} and $\mathbf{A}_{\text{im}} \in \mathbb{R}^{M \times N}$ being matrices defined elsewhere [26, 27]. We stress that the DRT-model, including the experimental state $\boldsymbol{\psi}$ is $(P + 1)$ -dimensional.

The experimental EIS data can also be written (compactly) as a vector, *i.e.*, $\mathbf{Z}_{\text{exp}}(\mathbf{f}, \boldsymbol{\psi}) = [Z_{\text{exp}}(f_1, \boldsymbol{\psi}), Z_{\text{exp}}(f_2, \boldsymbol{\psi}), \dots, Z_{\text{exp}}(f_M, \boldsymbol{\psi})]^\top$. We will assume that

$$\mathbf{Z}_{\text{exp}}(\mathbf{f}, \boldsymbol{\psi}) = \mathbf{Z}_{\text{DRT}}(\mathbf{f}, \boldsymbol{\psi}) + \boldsymbol{\varepsilon}(\boldsymbol{\psi}) \quad (4)$$

where $\boldsymbol{\varepsilon}(\boldsymbol{\psi}) \in \mathbb{R}^M$ is the experimental error with $\boldsymbol{\varepsilon}(\boldsymbol{\psi}) = \boldsymbol{\varepsilon}_{\text{re}}(\boldsymbol{\psi}) + i \boldsymbol{\varepsilon}_{\text{im}}(\boldsymbol{\psi})$ and $\boldsymbol{\varepsilon}_{\text{re}}, \boldsymbol{\varepsilon}_{\text{im}} \sim \sigma_n(\boldsymbol{\psi})\mathcal{N}(0, \mathbf{I})$ with $\mathbf{I} \in \mathbb{R}^{M \times M}$.

2.2 The Deep-DRT Neural Networks

As shown schematically in Figure 1, the deep-DRT model uses two feedforward DNNs: 1) an RL-net², whose parameters (*i.e.* biases and weights) are denoted as $\boldsymbol{\theta}_{\text{RL}}$; and 2) a γ -net, whose parameters are denoted as $\boldsymbol{\theta}_\gamma$. Following the rationale illustrated above, the inputs of the RL- and γ -nets are $\boldsymbol{\psi}$ and $[\log \boldsymbol{\tau}, \boldsymbol{\psi}]^\top$, respectively. The corresponding outputs are $[R_{\infty, \text{DNN}}(\boldsymbol{\psi}, \boldsymbol{\theta}_{\text{RL}}), L_{0, \text{DNN}}(\boldsymbol{\psi}, \boldsymbol{\theta}_{\text{RL}})]^\top$ and $\gamma_{\text{DNN}}(\log \boldsymbol{\tau}, \boldsymbol{\psi}, \boldsymbol{\theta}_\gamma)$. The network parameters $\boldsymbol{\theta}_{\text{RL}}$

² R and L stand for resistance and inductance, respectively.

and θ_γ can be obtained by minimizing of the following loss function derived from (2) with $\lambda = 0$:³

$$\begin{aligned} \mathcal{L}(\theta_{\text{RL}}, \theta_\gamma) = \sum_{\psi \in S_\psi} & \| \mathbf{z}_{\text{exp}}(\mathbf{f}, \psi) - i2\pi L_{0,\text{DNN}}(\psi, \theta_{\text{RL}}) \mathbf{f} - R_{\infty,\text{DNN}}(\psi, \theta_{\text{RL}}) \mathbf{1} \\ & - \mathbf{A} \gamma_{\text{DNN}}(\log \tau, \psi, \theta_\gamma) \|^2_2 \end{aligned} \quad (5)$$

where $\|\cdot\|_2$ indicates the 2-norm.

2.3 Implementation Details

Both the RL- and γ -nets were taken to be feedforward neural networks. The 8 layers of RL-net were: i) an input layer of dimension P , corresponding to the size of the state ψ ; ii) 6 hidden layers of width 10; and iii) an output layer of dimension 2, outputting $R_{\infty,\text{DNN}}(\psi)$ and $L_{0,\text{DNN}}(\psi)$ ⁴. The 8 layers of the γ -net were: i) an input layer as a vector of dimension $1 + P$, corresponding to the size of $[\log \tau, \psi]$; ii) 6 hidden layers of width 50; and iii) an output layer of dimension 1, giving $\gamma_{\text{DNN}}(\log \tau, \psi)$. The number of network parameters is reported in the supplementary information (SI), Table S1. For both RL- and γ -nets, non-saturating exponential linear units (ELUs) were utilized as the activation functions for the input and 6 hidden layers [54]. To ensure the positivity of the DRT, the softplus function was used at the output layer.

³ To simplify the notation, this formula assumes \mathbf{f} is independent of ψ . However, more generally, the frequency vector \mathbf{f} may be such that $\mathbf{f} = \mathbf{f}(\psi)$.

⁴ For the sake of clarity and to simplify the notation, the (explicit) dependence on the neural network parameters is omitted, unless needed.

All weights and biases were initialized using the Xavier uniform method and zero, respectively [47]. The Adam algorithm with a learning rate of 10^{-4} was used to minimize (5) with respect to θ_{RL} and θ_{γ} [55]. The maximum number of iterations was set to 3×10^5 . Early stopping was utilized to avoid overfitting [56], with the training process ending when the loss difference between two consecutive iterations was less than 10^{-8} . The implementation was done in PyTorch [57].

For all calculations, $\log \tau$ and ψ were min-max normalized to the $[-1, 1]$ and $[0, 1]$ intervals, respectively. To compute the \mathbf{A} matrix used to analyze artificial and perovskite solar cell experiments, the mid-point rule was utilized [26]. The Gaussian radial basis function (RBF) was used to discretize the DRT of the symmetric cell experiments [27].

For regression, training was done on $S_{\psi}^{\text{train}} = S_{\psi}$. For prediction, S_{ψ} was split into two equally sized training, S_{ψ}^{train} , and testing, S_{ψ}^{test} , subsets. During the analysis of artificial experiments, the relative error on γ , ε_{γ} , was tracked during the minimization of $\mathcal{L}(\theta_{\text{RL}}, \theta_{\gamma})$. At the q^{th} training iteration, $\varepsilon_{\gamma, q}$, is defined as

$$\varepsilon_{\gamma, q} = \sum_{\psi \in S_{\psi}^t} \left\| \gamma_{\text{DNN}}(\log \tau, \psi, \theta_{\gamma, q}) - \gamma_{\text{exact}}(\log \tau, \psi) \right\|_2 \quad (6)$$

where S_{ψ}^t is the specific dataset used for training (either S_{ψ}^{train} or, for regression, $S_{\psi}^{\text{regress}^5}$), $\theta_{\gamma, q}$ are the γ -net parameters (at the q^{th} training iteration) and $\gamma_{\text{exact}}(\log \tau, \psi)$ is the “exact” DRT.

2.4 Artificial Experiment Generation

⁵ “regress” stands for regression.

For all artificial experiments, the frequencies were selected to be in the 10^{-4} - 10^4 Hz interval with 10 points per decade (ppd) spacing consistent with our group's previous works [26, 27, 46]. The collocation points were chosen such that $\tau_n = 1/f_n$, implying $M = N$. Artificial experimental datasets, S_{ψ} , based on a scalar or 2D variables ψ (leading to 2D and 3D problems, respectively) were created by either gridding (uniform linear spacing) or randomly sampling artificial experimental points over $[0,1]$ or $[0,1] \times [0,1]$. If not stated otherwise, K was set to 11 ($\psi \in [0,1]$) or 121 ($\psi \in [0,1] \times [0,1]$), for regression, and 22 ($\psi \in [0,1]$) or 242 ($\psi \in [0,1] \times [0,1]$), for prediction, respectively. The model parameters (*e.g.* the charge transfer resistance R_{ct} and the timescale constant τ_0) were assumed to be affine or exponential functions of the state variables ψ .

The noise-corrupted artificial data were generated starting from the “exact” impedance models (Table 1 and from S2 to S5) by adding noise as illustrated in Section 2.1:

$$\mathbf{Z}_{\text{exp}}(\mathbf{f}, \psi) = \mathbf{Z}_{\text{exact}}(\mathbf{f}, \psi) + \boldsymbol{\varepsilon}(\psi) \quad (7)$$

where the diagonal elements of the covariance matrix of $\boldsymbol{\varepsilon}(\psi)$ are given by

$$\sigma_n^2(\psi) = \sigma_{n,0}^2 \rho(\psi) \quad (8)$$

where $\sigma_{n,0}^2$ is a scalar and $\rho(\psi)$ is a function dependent on ψ .

2.5 Assessment of the deep-DRT Model Performance

To visualize parameter-dependent analytical and estimated DRTs, we normalized DRT relative to the charge transfer resistance as detailed in Section 2.5.1. Regression and prediction performance were quantified by the relative errors and discrepancies of the EIS fitting as defined in Section 2.5.2.

2.5.1 Normalized DRT

The normalized DRT, $\gamma_{\text{DNN},\text{norm}}(\log \tau, \boldsymbol{\psi})$, is defined as

$$\gamma_{\text{DNN},\text{norm}}(\log \tau, \boldsymbol{\psi}) = \frac{1}{R_{\text{ct,DNN}}(\boldsymbol{\psi})} \gamma_{\text{DNN}}(\log \tau, \boldsymbol{\psi}) \quad (9)$$

where the normalization factor $R_{\text{ct,DNN}}(\boldsymbol{\psi})$ is the numerical integral of $\gamma_{\text{DNN}}(\log \tau, \boldsymbol{\psi})$ with respect to $\log \tau$.

2.5.2 Relative Errors and Discrepancies for Regression and Prediction

To evaluate regression and prediction performance, we used relative errors and discrepancies as metrics. The relative error, $\varepsilon_Z(f, \boldsymbol{\psi})$, on Z is defined as

$$\varepsilon_Z(f, \boldsymbol{\psi}) = \frac{|Z_{\text{DRT}}(f, \boldsymbol{\psi}) - Z_{\text{exact}}(f, \boldsymbol{\psi})|}{|Z_{\text{exact}}(f, \boldsymbol{\psi})|} \quad (10)$$

with the average minimum, average, and average maximum ε_Z defined as

$$\varepsilon_{Z,\min}^t = \frac{1}{K_t} \sum_{\boldsymbol{\psi} \in S_{\boldsymbol{\psi}}^t} \min_{f \in \mathcal{f}} \varepsilon_Z(f, \boldsymbol{\psi}) \quad (11a)$$

$$\varepsilon_{Z,\text{avg}}^t = \frac{1}{MK_t} \sum_{\boldsymbol{\psi} \in S_{\boldsymbol{\psi}}^t} \sum_{m=1}^M \varepsilon_Z(f_m, \boldsymbol{\psi}) \quad (11b)$$

$$\varepsilon_{Z,\max}^t = \frac{1}{K_t} \sum_{\boldsymbol{\psi} \in S_{\boldsymbol{\psi}}^t} \max_{f \in \mathcal{f}} \varepsilon_Z(f, \boldsymbol{\psi}) \quad (11c)$$

where $t = \text{regress, train, or test}$ ($S_{\boldsymbol{\psi}}^{\text{regress}} = S_{\boldsymbol{\psi}}$ and $S_{\boldsymbol{\psi}}^{\text{train}}, S_{\boldsymbol{\psi}}^{\text{test}} \subset S_{\boldsymbol{\psi}}$), and K_t is the cardinality of $S_{\boldsymbol{\psi}}^t$.

Analogously, we defined the relative discrepancy, $d_Z(f, \boldsymbol{\psi})$, between model and experiment as

$$d_Z(f, \boldsymbol{\psi}) = \frac{|Z_{\text{DRT}}(f, \boldsymbol{\psi}) - Z_{\text{exp}}(f, \boldsymbol{\psi})|}{|Z_{\text{exp}}(f, \boldsymbol{\psi})|} \quad (12)$$

with corresponding average minimum, average, and average maximum d_Z given by

$$d_{Z,\min}^t = \frac{1}{K_t} \sum_{\boldsymbol{\psi} \in S_{\boldsymbol{\psi}}^t} \min_{f \in f} d_Z(f, \boldsymbol{\psi}) \quad (13a)$$

$$d_{Z,\text{avg}}^t = \frac{1}{MK_t} \sum_{\boldsymbol{\psi} \in S_{\boldsymbol{\psi}}^t} \sum_{m=1}^M d_Z(f_m, \boldsymbol{\psi}) \quad (13b)$$

$$d_{Z,\max}^t = \frac{1}{K_t} \sum_{\boldsymbol{\psi} \in S_{\boldsymbol{\psi}}^t} \max_{f \in f} d_Z(f, \boldsymbol{\psi}) \quad (13c)$$

3 Artificial Experiments

We first tested the model on several artificial 2D datasets dependent on a single scalar state ψ (*i.e.* 2D EIS data), including a single ZARC model [3, 58]; 2×ZARC with overlapping and discontinuous (*i.e.* fractal [58] and piecewise constant (PWC) [24]) timescale distributions, a simulated symmetric lithium ionic battery (LIB). As a second step, we tested a ZARC model using 3D datasets, whose experimental state is characterized on two state variables (*i.e.* $\boldsymbol{\psi} = [\psi_1, \psi_2]^\top$).

3.1 ZARC Model

We studied a ZARC model [3], consisting of an ohmic resistor, R_∞ , in series with a circuit comprising a resistor, R_{ct} , in parallel with a constant phase element with the characteristic time τ_0 (Table 1). The parameters of the artificial experiments can be found in Table S2.

3.1.1 Regression

3.1.1.1 Charge Transfer Resistance (R_{ct}) Affinely Dependent on the State Variable

The R_{ct} was assumed to be affinely dependent on ψ , *i.e.*,

$$R_{\text{ct}}(\psi) = R_{\text{ct},0} + (R_{\text{ct},1} - R_{\text{ct},0})\psi \quad (14)$$

where $R_{\text{ct},0}$ and $R_{\text{ct},1}$ are scalars whose values are given in Table S2.

The experimental dataset S_ψ contains 11 equispaced ψ 's from 0 to 1 (boundaries included).

Using (8), we set $\sigma_{n,0} = 1 \, \Omega$ and

$$\rho(\psi) = 1 + \left(\frac{R_{\text{ct},1} - R_{\text{ct},0}}{R_{\text{ct},1}} \right) \psi \quad (15)$$

We obtained a close fit of the EIS spectra, see Figure 2 (a) and S1 in the SI. The correspondingly deconvolved $\gamma_{\text{DNN}}(\log \tau, \psi)$'s closely capture the exact DRTs as shown in Figure 2 (b). By integrating $\gamma_{\text{DNN}}(\log \tau, \psi)$ numerically with respect to $\log \tau$ we estimated $R_{\text{ct}}(\psi)$, whose value, $R_{\text{ct,DNN}}(\psi)$, matches closely the “exact” one, $R_{\text{ct,exact}}(\psi)$ (Figure 2 (c)). The normalized DRT, see (9), is shown in the contour plot reported in Figure 2 (d) where it is apparent that the deconvolved $\gamma_{\text{DNN,norm}}(\log \tau, \psi)$ is independent of ψ , consistent with the 2D model used.

3.1.1.2 Timescale (τ_0) Exponentially Dependent on the State Variable

For the second set of artificial experiments, we assumed the $\tau_0(\psi)$ of the ZARC to depend exponentially on ψ with

$$\tau_0(\psi) = \tau_{0,0} e^{\psi \log \frac{\tau_{0,1}}{\tau_{0,0}}} \quad (16)$$

where $\tau_{0,0}$ and $\tau_{0,1}$ are two scalars whose values are given in Table S2. The artificial dataset S_ψ contains 11 equispaced ψ 's from 0 to 1 (boundaries included).

We achieved a satisfactory fit of the artificial EIS spectra, as seen in the Nyquist (Figure S2) and Bode diagrams of Figure 3 (a) and (b), respectively. As shown in Figure 3 (c), $\gamma_{\text{DNN}}(\log \tau, \psi)$'s (blue lines) and corresponding exact DRTs (black lines) match well. Moreover, as shown in Figure 3(d), $\gamma_{\text{norm,DNN}}(\log \tau, \psi)$'s peaks shift towards the right according to (16), as ψ increases, with no shape change, consistent with the assumption $R_{\text{ct}}(\psi) = \text{constant}$.

3.1.1.3 Affinely Dependent R_{ct} and Exponentially Dependent τ_0

We summed up the two effects studied in the previous sections by setting $R_{\text{ct}}(\psi)$ and $\tau_0(\psi)$ to follow (14) and (16), respectively. Figure S3 (a) and (b) shows “experimental”, exact, and recovered EIS spectra and DRTs. $R_{\text{ct}}(\psi)$'s and $\gamma_{\text{norm,DNN}}(\log \tau, \psi)$'s are reported in Figure S3 (c) and (d). The Bode diagrams can be found in Figure S4. All properties are captured well by the 2D deep-DRT model.

3.1.1.4 Evolution of the Loss Function and DRT Error During Training

For the three artificial experiments described in the preceding sections, we tracked the loss and relative error with the corresponding plots shown in Figure 4 (a) to (c). During training, $\mathcal{L}(\theta_{\text{RL}}, \theta_\gamma)$ consistently reached its minimum in less than 15,000 iterations. The ε_γ decreased past that threshold finally reaching some minimum later. Continuing the training after the minimum led to an increase in ε_γ . From Figure S5, it is apparent that all EIS data were well regressed at the early stopping iteration.

3.1.2 Prediction with Randomly Sampled Experimental State

The ZARC model was then tested against prediction. We used the same models studied in regression (see Section 3.1.1) with the difference that, to demonstrate no specific spacing/gridding on ψ is required, we generated the 22 elements of S_ψ using a uniform distribution, *i.e.*, $S_\psi \ni \psi \sim U(0,1)$. S_ψ was split into two identically sized training, S_ψ^{train} , and test, S_ψ^{test} , subsets, see Figure 5 (c). For the test dataset, the trained 2D deep-DRT model accurately predicted EIS data and corresponding DRTs, obtaining estimated $R_{\text{ct,DNN}}(\psi)$ and $\gamma_{\text{norm,DNN}}(\log \tau, \psi)$ consistent with the exact values $R_{\text{ct,exact}}(\psi)$ and $\gamma_{\text{exact}}(\log \tau, \psi)$ (Figures 5, S6 and S7). Relative errors and discrepancies, as defined by (11) and (13) in Section 2.5.2, were small for both regression and prediction (Table S6).

3.1.3 Uncertainty Quantification

For the example in Section 3.1.1.1, we used two methods to estimate the confidence interval of the deconvolved deep-DRT. In the first (brute-force) approach, 10 artificial experimental datasets were generated starting from identical “exact” parameters. Then regression was carried out to obtain the 10 corresponding deep-DRT models. Second, the dataset of Section 3.1.1.1 was used to repeat the analysis therein for 10 sets of randomly chosen weights and biases. For the two cases, mean DRTs and “error bars” are reported in Figure S8 ($\psi = 0.5$). Relative errors and discrepancies, as defined by (11) and (13) in Section 2.5.2, are reported in Table S7. Interestingly, both methods not only suggest that the deep-DRT method is robust, but they also yielded similar results, implying that randomly choosing weights and biases has the potential to quantify uncertainty of deep-DRT models.

3.2 2×ZARC Model

In real electrochemical systems, several physical processes may occur simultaneously, making timescale separation challenging. In this regard, we tested whether the deep-DRT can capture

overlapping DRT features typical of 2×ZARC models. EIS model and corresponding DRT equations can be found in Table 1. Model parameters are given in Table S3. The 2×ZARC parameters are denoted as $(R_{ct,1}, \tau_1, \phi_1)$ and $(R_{ct,2}, \tau_2, \phi_2)$, respectively, where the first ZARC was taken to be independent of ψ . We studied two datasets generated by taking the second ZARC with the following dependence on ψ : 1) affine for $R_{ct,2}$ and independent of τ_2 ; and 2) affine for $R_{ct,2}$ and exponential for τ_2 . The Nyquist and Bode plots, the recovered DRTs, the total charge transfer resistance $R_{ct}(\psi) = R_{ct,1} + R_{ct,2}(\psi)$, and $\gamma_{DNN, \text{norm}}(\log \tau, \psi)$ are shown in Figures S9 and S10, for dataset 1), and Figures S11 and S12, for dataset 2). In both cases, “experimental” 2D EIS spectra were closely regressed by the 2D deep-DRT model obtaining an excellent deconvolution of the DRT.

3.3 Spectra with Discontinuous DRTs

We tested whether the deep-DRT method can recover discontinuous DRTs. Consequently, fractal [26] and PWC [24] elements were studied (see Table 1), where $R_{ct}(\psi)$ followed (14) and τ_0 was independent of ψ . Model parameters can be found in Table S4. For both cases, the 2D EIS spectra were recovered well and $R_{ct}(\psi)$ was accurately estimated. The $\gamma_{DNN, \text{norm}}(\log \tau, \psi)$ are shown in Figure S13 (c) and (f). In addition, the $\gamma_{DNN}(\log \tau, \psi)$ captured the DRT as shown in Figure S14, where the reduced accuracy near the discontinuities is attributed to a low collocation point density.

3.4 Symmetric LIB Model

To expand our study to a more realistic system, we used a modified version of the symmetric LIB model of Watanabe and coworkers [59]. The corresponding ECM can be found in Figure S15 and the $Z_{\text{exact}}(f, T)$ is reported in Table 1. As shown in Figure S15, the ECM consists of

two nested parallel ZARCs, with parameters given in Table S8. The resistances $R_{\text{ct}}(T)$, and $R_{\text{b}}(T)$ follow an Arrhenius-type relation [59], whose parameters are given in Table S8, *i.e.*,

$$R_{\text{ct}}(T) = R_{\text{ct},0} \exp \left(\frac{E_{\text{act,ct}}}{k_{\text{B}}T} \right) \quad (17a)$$

$$R_{\text{b}}(T) = R_{\text{b},0} \exp \left(\frac{E_{\text{act,b}}}{k_{\text{B}}T} \right) \quad (17b)$$

where k_{B} is the Boltzmann constant, $R_{\text{ct},0}$ and $R_{\text{b},0}$ are pre-exponential terms, and $E_{\text{act,ct}}$ and $E_{\text{act,b}}$ are the activation energies for R_{ct} and R_{b} , respectively. Different from the previous artificial experiments, an analytical expression of the exact DRT is not available. Therefore, the exact DRT was computed from $Z_{\text{exp}}(f, T)$ using the formula given in Table 1 [24, 60].

3.4.1 Regression

We generated S_{ψ} by selecting 31 equispaced $\psi = \frac{T-T_{\text{min}}}{T_{\text{max}}-T_{\text{min}}}$ in the $[0, 1]$ interval (boundaries included). Artificial experiments were generated according to (7). The noise $\varepsilon(\psi)$ was defined by (8) with $\sigma_{n,0} = 100 \Omega$ and

$$\rho(\psi) = 1 + \left(\frac{\rho_{\text{max}} - \rho_0}{\rho_0} \right) \psi \quad (18)$$

where $\rho_0 = 1$ and $\rho_{\text{max}} = 0.1$.

Frequencies were selected to be in the 10^{-2} - 10^7 Hz interval with 10 ppd. We obtained a close fit of the EIS spectra against the artificial experiments and deconvolved $\gamma_{\text{DNN}}(\log \tau, T)$, see Figure S16 (a) and (b). As shown in Figure S16 (d) and (f), $\gamma_{\text{DNN,norm}}(\log \tau, T)$ shows two distinct peaks (in the 10^{-7} - 10^{-4} s and 10^{-3} - 10^0 s subintervals), which correspond to the time constants $\tau_{\text{e}}(T) = R_{\text{ct}}(T)^{\frac{1}{\phi_{\text{e}}}} Q_{\text{e}}$ and $\tau_{\text{g}}(T) = R_{\text{b}}(T)^{\frac{1}{\phi_{\text{g}}}} Q_{\text{g}}$. It should be noted that $\tau_{\text{e}}(T)$ and

$\tau_g(T)$ depend exponentially on ψ because Q_e and Q_g are assumed to be constant in the investigated temperature range [59].

3.4.2 Prediction

We generated S_ψ by taking 62 uniform samples of $\psi = \frac{T-T_{\min}}{T_{\max}-T_{\min}}$ in the $[0,1]$ interval. S_ψ was split into two identically sized training S_ψ^{train} and test S_ψ^{test} subsets. Using the trained deep-DRT model, we successfully predicted the DRTs and estimated the corresponding $Z_{\text{DRT}}(f, T)$ in the test subset. The model EIS spectra matched the corresponding experimental data (Figure S17a). Further, the DRTs' peak location and heights were consistent with those obtained using the training dataset (Figure S16). Average relative errors, $\varepsilon_{Z,\text{avg}}^{\text{test}}$, and discrepancies, $d_{Z,\text{avg}}^{\text{test}}$, defined by (11b) and (13b), were less than 6% and 7% for the test dataset, respectively, see Table S9.

3.5 ZARC Model Dependent on Two State Variables

We investigated whether the deep-DRT can capture 3D data, which depends on f and the 2D experimental state vector $\boldsymbol{\psi} = [\psi_1, \psi_2]^\top$. We considered the single ZARC model of Section 3.1 with either $R_{\text{ct}}(\boldsymbol{\psi}) = R'_{\text{ct}}(\psi_1) + R''_{\text{ct}}(\psi_2)$ or $\tau_0(\boldsymbol{\psi}) = \tau'_0(\psi_1) + \tau''_0(\psi_2)$, where $R'_{\text{ct}}(\psi_1)$, $R''_{\text{ct}}(\psi_2)$, $\tau'_0(\psi_1)$, and $\tau''_0(\psi_2)$ were calculated using (14) or (16) for affinely and exponentially dependent datasets, respectively.

3.5.1 Regression

For regression, we studied three datasets generated by taking: 1) $R_{\text{ct}}(\boldsymbol{\psi})$ to be exponentially dependent on both ψ_1 and ψ_2 (*i.e.* $R_{\text{ct}}(\boldsymbol{\psi}) = R'_{\text{ct}}(\psi_1) + R''_{\text{ct}}(\psi_2)$ where $R'_{\text{ct}}(\psi_1) = R_{\text{ct},0,1} e^{\psi_1 \log \frac{R_{\text{ct},1,1}}{R_{\text{ct},0,1}}}$ and $R''_{\text{ct}}(\psi_2) = R_{\text{ct},0,2} e^{\psi_2 \log \frac{R_{\text{ct},1,2}}{R_{\text{ct},0,2}}}$); 2) $R_{\text{ct}}(\boldsymbol{\psi})$ affinely dependent on ψ_1 and

exponentially dependent on ψ_2 (*i.e.* $R_{\text{ct}}(\boldsymbol{\psi}) = R'_{\text{ct}}(\psi_1) + R''_{\text{ct}}(\psi_2)$ where $R'_{\text{ct}}(\psi_1) = R_{\text{ct},0,1} + (R_{\text{ct},1,1} - R_{\text{ct},0,1})\psi_1$ and $R''_{\text{ct}}(\psi_2) = R_{\text{ct},0,2}e^{\psi_2 \log \frac{R_{\text{ct},1,2}}{R_{\text{ct},0,2}}}$; and 3) $\tau_0(\boldsymbol{\psi})$ exponentially dependent on ψ_1 and affinely dependent on ψ_2 (*i.e.* $\tau_0(\boldsymbol{\psi}) = \tau'_0(\psi_1) + \tau''_0(\psi_2)$ where $\tau'_0(\psi_1) = \tau_{0,0,1}e^{\psi_1 \log \frac{\tau_{0,1,1}}{\tau_{0,0,1}}}$ and $\tau''_0(\psi_2) = \tau_{0,0,2} + (\tau_{0,1,2} - \tau_{0,0,2})\psi_2$). The artificial experiment dataset, $S_{\boldsymbol{\psi}}$, was created by taking 121 uniformly gridded $\boldsymbol{\psi}$ in $[0,1] \times [0,1]$. The model parameters can be found in Table S5.

Artificial EIS spectra were regressed using the deep-DRT method with the corresponding DRTs deconvolved satisfactorily (Figures from S18 to S23). For datasets 1) and 2), $\gamma_{\text{DNN,norm}}(\log \tau, \boldsymbol{\psi})$ and $R_{\text{ct}}(\boldsymbol{\psi})$ were closely recovered, as shown in Figures S18, S19, and S20. For dataset 3), the dependence on $\tau_0(\boldsymbol{\psi})$ of the deconvolved $\gamma_{\text{DNN}}(\log \tau, \boldsymbol{\psi})$ was captured successfully (Figure S22 (a) and (c), and Figure S23 (a) and (c)). When $\psi_1 = 0$, then $\tau'_0(0) = \tau_{0,0,1} \ll \tau''_0(\psi_2)$, the linear dependence (dashed line) of $\gamma_{\text{DNN,norm}}(\log \tau, \boldsymbol{\psi})$ on ψ_2 was recovered (Figure S22 (b)). Conversely, when $\psi_1 = 1$, $\tau'_0(1) = \tau_{0,1,1} \gg \tau''_0(\psi_2)$, the $\gamma_{\text{DNN,norm}}(\log \tau, \boldsymbol{\psi})$ was correctly shown to be independent on ψ_2 (Figure S22 (d)). Moreover, when ψ_2 was fixed to either 0 (Figure S23 (a)) or 1 (Figure S23 (c)), the DRT peaks were recovered, see Figure S23 (b) and (d), respectively.

3.5.2 Prediction

We simulated the first dataset of Section 3.5.1 (*i.e.* $R_{\text{ct}}(\boldsymbol{\psi}) = R_{\text{ct},0}e^{\psi_1 \log \frac{R_{\text{ct},1}}{R_{\text{ct},0}}} + R_{\text{ct},0}e^{\psi_2 \log \frac{R_{\text{ct},1}}{R_{\text{ct},0}}}$) again. We generated an $S_{\boldsymbol{\psi}}$ with 242 elements chosen such that $\psi_1, \psi_2 \sim U(0,1)$. We split $S_{\boldsymbol{\psi}}$ into two identically sized training, $S_{\boldsymbol{\psi}}^{\text{train}}$, and test, $S_{\boldsymbol{\psi}}^{\text{test}}$, subsets. Figure 6 (a), (b) and (c) report fitted EIS data, $\gamma_{\text{DNN}}(\log \tau, \boldsymbol{\psi})$ for a $\boldsymbol{\psi} \in S_{\boldsymbol{\psi}}^{\text{test}}$, and estimated

$R_{\text{ct}}(\boldsymbol{\psi})$ with the distribution of points for both training and test datasets, respectively. As shown in Figure 6, the trained model accurately fitted the 3D synthetic EIS spectra and predicted the corresponding DRTs of the test dataset.

Average relative errors, $\varepsilon_{Z,\text{avg}}^{\text{train}}$ and $\varepsilon_{Z,\text{avg}}^{\text{test}}$, and discrepancies, $d_{Z,\text{avg}}^{\text{train}}$ and $d_{Z,\text{avg}}^{\text{test}}$, defined by (11b) and (13b), were less than 1% and 4%, respectively, as reported in Table S6, for both regression (dataset in Section 3.5.1) and prediction (test dataset).

4 Experiments

After testing the consistency of the deep-DRT method with artificial experiments, we assessed its performance against real experimental data. First, we analyzed the 4D EIS spectra of a symmetric cell which was tested as a function of cationic deficiency, x , temperature, T , and oxygen partial pressure, p_{O_2} . Second, we applied the deep-DRT to the 2D EIS data of a perovskite solar cell whose environment changed with time t . For the datasets considered, the timescales had 10 ppd in the 10^{-7} to 10^3 s range for the symmetric cell and in the 10^{-7} to 10^{-1} s range for the perovskite solar cell.

4.1 Symmetric Cell with SOFC Cathode Materials

4.1.1 Regression

We first studied the EIS of symmetric cells based on $(\text{Ba}_{0.95}\text{La}_{0.05})_{1-x}\text{FeO}_{3-\delta}$ (BLF-Dx) with samarium doped ceria (SDC) as the electrolyte and in the BLF-Dx|SDC|BLF-Dx configuration. The experimental impedance, $Z_{\text{exp}} = Z_{\text{exp}}(f, T, p_{\text{O}_2}, x)$, was measured between 10^{-2} and 5×10^5 Hz with 15 ppd. EIS spectra were obtained for $x = 0, 5, 10$, and 20%, $T = 500, 550, \dots, 700$ °C, and $p_{\text{O}_2} = 0.21, 0.40, 0.60, 0.80$, and 1 atm. Further experimental details are given in [61].

We first used the 3D deep-DRT model on the material having cationic deficiency 5% (BLF-D5), using the experimental state $\psi = [T, p_{\text{O}_2}]^T$ (*i.e.* a 3D dataset). The deep-DRT model was validated and benchmarked using an ECM found in the literature [62, 63], consisting of an inductor and an ohmic resistance in series with two ZARC elements. As shown in Figures 7, 8, and S25, both the deep-DRT and ECM models fitted the EIS data closely. The corresponding average discrepancies $d_{Z,\text{avg}}^{\text{regress}}$, defined in Section 2.5.2, were below 1% for both cases, see Table S10. Since the EIS arcs of the two ZARCs overlap, the DRTs display an asymmetric peak, as shown in Figures 7 (b), (d), and 8 (b). The total polarization resistance $R_{\text{tot}}(\psi)$, estimated by integrating $\gamma_{\text{DNN}}(\log \tau, \psi)$, is reduced by increasing T and p_{O_2} , see Figure 8 (c). The timescale constants τ_1 and τ_2 , estimated by the ECM, followed the $\gamma_{\text{norm,DNN}}(\log \tau, \psi)$ level lines (Figures 8 (d) and S26). We extended the analysis to BLF-Dx compositions with $x = 0, 10$, and 20% (BLF-D0, BLF-D10, and BLF-D20, respectively). As shown in Figures S24, S27, and S28, the EIS spectra closely recovered the experimental data, suggesting that the deep-DRT model also captures compositional dependence.

Finally, we tested the deep-DRT model with $\psi = [T, p_{\text{O}_2}, x]^T$ (*i.e.* 4D dataset) by regressing the EIS data of BLF-D5, BLF-D10, and BLF-D20 at $T = 600, 650$, and 700°C and $p_{\text{O}_2} = 0.21, 0.40, 0.60, 0.80$, and 1 atm . The 4D model closely recovered the experimental EIS data and deconvolved the corresponding DRTs (Figure S29). DRT estimates obtained are close for all the timescales (Figures 9 and S29).

4.1.2 Prediction

We tested both 3D and 4D datasets against the prediction of EIS spectra and corresponding DRTs. The 3D training dataset contained the BLF-D5 data at $T = 500, 600$, and 700°C , and $p_{\text{O}_2} = 0.21, 0.40, 0.60, 0.80$, and 1 atm . Testing was done for BLF-D5 at $T = 550$ and 650°C

and all p_{O_2} 's. The 4D dataset contained the EIS spectra for $x = 5, 10, 20 \%$, $T = 600, 650, 700^\circ\text{C}$ and all p_{O_2} 's, with training done at $T = 600$ and 700°C and testing at $T = 650^\circ\text{C}$. As shown in Figures 9 and S29, the deep-DRT models, trained with 3D and 4D EIS datasets, predicted the EIS spectra and the corresponding DRTs with satisfactory accuracy. Specifically, the average discrepancies $d_{Z, \text{avg}}^{\text{test}}$ on the test dataset were less than 1.5% and 6.5% (Table S11) for the 3D and 4D model, respectively.

4.2 Perovskite Solar Cell

As an additional experimental example, we studied the EIS data of a perovskite solar cell. The perovskite solar cell configuration was FTO glass/ SnO_2 /(FAPbI_3)_{0.85}(MAPbBr_3)_{0.15}/Spiro – OMeTAD/Au. FTO refers to fluorine-doped tin oxide, SnO_2 is a electron-transport layer, (FAPbI_3)_{0.85}(MAPbBr_3)_{0.15} is a mixed perovskite absorber, and Spiro – OMeTAD is a hole-transport layer. Further details regarding the preparation methods of the sample are given elsewhere [64].

EIS spectra were recorded with 10 ppd spacing from 10^0 and 5×10^6 Hz under various atmospheric conditions. The operating atmospheric condition first gradually changed from 1 atm of pure N_2 to 1 atm of pure O_2 (group 1), then moved back to ambient air, *i.e.*, 21% O_2 and 79% N_2 , with a relative humidity of $\sim 40\%$ (group 2), and finally returned to pure N_2 (group 3). To apply the deep-DRT model, we set as state variable the time t . The time schedules of each group of experiments are reported in [64].

We employed a suitable ECM found in the literature to validate the deep-DRT model results [52]. For group 1, EIS data were closely fitted, and the deconvolved DRT of both the ECM and deep-DRT model are similar (see Figure 10 (a) and (b)). The total polarization resistance R_{tot} remarkably decreased as t passed. Specifically, increasing p_{O_2} reduced $R_{\text{tot}}(t)$ for the first 40

mins, followed by a slight increase (see Figure 10 (c)). Meanwhile, $\gamma_{\text{DNN, norm}}(\log \tau, t)$'s peak narrowed with its position unchanged at 10^{-3} s (see Figure 10 (d)).

For groups 2 and 3, EIS data and corresponding DRTs can be found in Figures S30 and S31, respectively. Upon reversing the atmospheric conditions (*i.e.* group 2), $R_{\text{tot}}(t)$ sharply increased in the first 70 min, then $R_{\text{tot}}(t)$ stayed stable for 20 min, and finally decreased. $\gamma_{\text{DNN, norm}}(\log \tau, t)$'s peak at 10^{-3} s shrank, and a new peak at 10^{-1} s appeared. Furthermore, returning to the initial condition (*i.e.* group 3) leads to an instant drop of $R_{\text{tot}}(t)$ followed by a mild increase. Nonetheless, $\gamma_{\text{DNN, norm}}(\log \tau, t)$ did not change significantly. Comparing the Bode diagrams, both 2D deep-DRT and ECM models catch the magnitude of the impedance accurately. However, the ECM fitted the phase of the EIS slightly better at high frequencies.

5 Conclusions

This article proposes the deep-DRT method, which encodes EIS data in a DNN dependent on the frequencies and experimental state at which EIS data are collected. Analysis of artificial data, collected for the various (multidimensional) experimental states, ψ , shows that the deep-DRT can accurately and consistently deconvolve the DRT even for challenging spectra characterized overlapping or discontinuous timescale distributions. Furthermore, the deep-DRT was gainfully used to analyze EIS data taken at randomly sampled experimental states. Further, the deep-DRT model performed well against experimental EIS data from SOFC cathode materials in a symmetric cell configuration and a perovskite solar cell, showing both regressive and prediction ability.

The promising results presented in this article suggest that the deep-DRT method may be suitable for the analysis of EIS spectra of complex electrochemical systems (*e.g.* supercapacitors, flow batteries, electrolyzers, etc.), which may depend on several “unstructured”

state variables. This work opens the path to deconvolving EIS data through DNNs encoding both frequency and experimental state dependence.

Acknowledgments

The authors gratefully acknowledge the Research Grant Council of Hong Kong for support through the projects (16204517, 16201820, and 16206019). E. Quattrocchi, S. Pepe, and A. Belotti thank the Hong Kong Ph.D. Fellowship Scheme for the support.

List of Acronyms

Acronym	Description
BLF-Dx	$(\text{Ba}_{0.95}\text{La}_{0.05})_{1-x}\text{FeO}_{3-\delta}$
DNN	Deep neural network
deep-DRT	Distribution of relaxation times deconvolved with a deep-neural network
DP-DRT	Deep-prior distribution of relaxation times
DRT	Distribution of relaxation times
ECM	Equivalent circuit model
EIS	Electrochemical impedance spectroscopy
LIB	Lithium ion battery
PWC	Piecewise constant
RBF	Radial basis function
RR	Ridge regression
SDC	Samarium-doped ceria
SI	Supplementary information
SOFC	Solid oxide fuel cell

List of Symbols

Variable	Description	Unit
\mathbf{A}	$\mathbf{A}_{\text{re}} + i\mathbf{A}_{\text{im}}$	-
\mathbf{A}_{im}	Imaginary DRT matrix	-
\mathbf{A}_{re}	Real DRT matrix	-
$d_z(f, \boldsymbol{\psi})$	Discrepancy at f and $\boldsymbol{\psi}$.	-
$d_z(\boldsymbol{\psi})$	Average relative discrepancy at state $\boldsymbol{\psi}$.	-
$d_{z,\text{avg}}^t$	Average discrepancy in $S_{\boldsymbol{\psi}}^t$. ($t = \text{regress, train, or test}$).	-
$d_{z,\text{max}}^t$	Average maximum discrepancy in $S_{\boldsymbol{\psi}}^t$. ($t = \text{regress, train, or test}$).	-
$d_{z,\text{min}}^t$	Average minimum discrepancy in $S_{\boldsymbol{\psi}}^t$. ($t = \text{regress, train, or test}$).	-
f	Frequency	Hz
\mathbf{f}	Frequency vector	Hz
\mathbf{I}	Identity matrix	-
K	Number of samples in the experimental dataset	-
K_t	Number of samples in the training or test dataset	-
$L_0(\boldsymbol{\psi})$	Inductance as a function of the experimental state $\boldsymbol{\psi}$.	H
$L_{0,\text{DNN}}(\boldsymbol{\psi}, \boldsymbol{\theta}_{\text{RL}})$	Inductance from the DNN and the RL network parameters.	H
\mathbf{L}	Differentiation matrix	-

$\mathcal{L}(\boldsymbol{\gamma}, \lambda)$	Loss as a function of the DRT vector, $\boldsymbol{\gamma}$, and penalty parameter, λ .	Ω^2
$\mathcal{L}(\boldsymbol{\theta}_{\text{RL}}, \boldsymbol{\theta}_{\gamma})$	Loss function written as a function of the neural network parameters	Ω^2
M	Number of exponential frequencies	-
N	Number of τ collocation points used to approximate $\gamma(\log \tau)$	-
P	Number of state variables (<i>i.e.</i> $\boldsymbol{\psi} \in \mathbb{R}^P$)	-
$P(\boldsymbol{\gamma})$	Penalty used for regularization	Ω^2
p_{O_2}	Oxygen partial pressure	atm
q	Training iteration	-
$R_{\text{ct}}(\boldsymbol{\psi})$	Charge transfer resistance	Ω
$R_{\text{ct,exact}}(\boldsymbol{\psi})$	Exact charge transfer resistance	Ω
$R_{\text{ct,DNN}}(\boldsymbol{\psi})$	Estimated charge transfer resistance	Ω
$R_{\infty}(\boldsymbol{\psi})$	Ohmic resistance	Ω
$R_{\infty,\text{DNN}}(\boldsymbol{\psi}, \boldsymbol{\theta}_{\text{RL}})$	Estimated Ohmic resistance	Ω
S_{ψ}	Experimental dataset	-
S_{ψ}^t	Regression, training or test dataset	-
t	Time	s
T	Temperature (absolute)	K
x	Cation deficiency of BLF-Dx	-
$Z_{\text{DRT}}(f)$	EIS estimated with the DRT model	Ω
$Z_{\text{DRT}}(f, \boldsymbol{\psi})$	EIS estimated with the deep-DRT model at $\boldsymbol{\psi}$	Ω

$\mathbf{Z}_{\text{DRT}}(\mathbf{f}, \boldsymbol{\psi})$	Discretized EIS estimated with the deep-DRT model at $\boldsymbol{\psi}$	Ω
$Z_{\text{exact}}(\mathbf{f}, \boldsymbol{\psi})$	Analytical impedance at $\boldsymbol{\psi}$	Ω
$Z_{\text{exp}}(\mathbf{f}, \boldsymbol{\psi})$	Experimental impedance at $\boldsymbol{\psi}$	Ω
$\gamma(\log \tau, \boldsymbol{\psi})$	Analytical DRT at $\boldsymbol{\psi}$	Ω
$\boldsymbol{\gamma}(\log \tau, \boldsymbol{\psi})$	Discretized analytical DRT at $\boldsymbol{\psi}$	Ω
$\gamma_{\text{DNN}}(\log \tau, \boldsymbol{\psi})$	DRT function estimated with the deep-DRT at $\boldsymbol{\psi}$	Ω
$\boldsymbol{\gamma}_{\text{DNN}}(\log \tau, \boldsymbol{\psi})$	Discretized DRT function estimated with the deep-DRT at $\boldsymbol{\psi}$	
$\gamma_{\text{DNN,norm}}(\log \tau, \boldsymbol{\psi})$	Normalized $\gamma_{\text{DNN}}(\log \tau, \boldsymbol{\psi})$	-
$\boldsymbol{\varepsilon}(\boldsymbol{\psi})$	Experimental error vector	Ω
$\boldsymbol{\varepsilon}_{\text{re}}(\boldsymbol{\psi})$	Real part of $\boldsymbol{\varepsilon}(\boldsymbol{\psi})$	Ω
$\boldsymbol{\varepsilon}_{\text{im}}(\boldsymbol{\psi})$	Imaginary part of $\boldsymbol{\varepsilon}(\boldsymbol{\psi})$	Ω
ε_{γ}	Relative error on γ	Ω
$\varepsilon_{\gamma,q}$	Relative error on γ at the iteration q	Ω
$\varepsilon_Z(\mathbf{f}, \boldsymbol{\psi})$	Relative error at \mathbf{f} and state $\boldsymbol{\psi}$	-
$\varepsilon_Z(\boldsymbol{\psi})$	Average relative error at state $\boldsymbol{\psi}$	-
$\varepsilon_{Z,\text{avg}}^t$	Average relative error in $S_{\boldsymbol{\psi}}^t$ ($t = \text{regress, train, or test}$)	-
$\varepsilon_{Z,\text{max}}^t$	Average maximum relative error in $S_{\boldsymbol{\psi}}^t$ ($t = \text{regress, train, or test}$)	-
$\varepsilon_{Z,\text{min}}^t$	Average minimum relative error in $S_{\boldsymbol{\psi}}^t$ ($t = \text{regress, train, or test}$)	-

θ_{RL}	Parameters of the RL-net (<i>i.e.</i> biases and weights)	-
θ_{γ}	Parameters of the γ -net (<i>i.e.</i> biases and weights)	-
λ	Penalty parameter	-
$\rho(\psi)$	Variance scaling	-
$\sigma_{n,0}$	Standard deviation pre-factor	Ω
$\sigma_n(\psi)$	Standard deviation of the experimental error	Ω
τ	Characteristic relaxation timescale	s
$\boldsymbol{\tau}$	Vector of characteristic relaxation timescales	s
ϕ	Exponent of the constant phase element	-
ψ	State variable vector	-

Table 1 – “Exact” impedances and DRTs used for the artificial experiments. ($H(\tau)$ is the Heaviside function)

Model	$Z(f, \boldsymbol{\psi})$	$\gamma(f, \boldsymbol{\psi})$	Reference
ZARC	$R_\infty + \frac{R_{ct}(\boldsymbol{\psi})}{1 + (i2\pi f\tau_0(\boldsymbol{\psi}))^\phi}$	$\frac{R_{ct}(\boldsymbol{\psi})}{2\pi} \frac{\sin((1-\phi)\pi)}{\cosh\left(\phi \log\left(\frac{\tau}{\tau_0(\boldsymbol{\psi})}\right)\right) - \cos((1-\phi)\pi)}$	[3]
2×ZARC	$R_\infty + \frac{R_{ct,1}(\boldsymbol{\psi})}{1 + (i2\pi f\tau_1(\boldsymbol{\psi}))^{\phi_1}} + \frac{R_{ct,2}(\boldsymbol{\psi})}{1 + (i2\pi f\tau_2(\boldsymbol{\psi}))^{\phi_2}}$	$\frac{R_{ct,1}(\boldsymbol{\psi})}{2\pi} \sin((1-\phi_1)\pi) \left(\frac{1}{\cosh\left(\phi_1 \log\left(\frac{\tau}{\tau_1(\boldsymbol{\psi})}\right)\right) - \cos((1-\phi_1)\pi)} \right) + \frac{R_{ct,2}(\boldsymbol{\psi})}{2\pi} \sin((1-\phi_2)\pi) \left(\frac{1}{\cosh\left(\phi_2 \log\left(\frac{\tau}{\tau_2(\boldsymbol{\psi})}\right)\right) - \cos((1-\phi_2)\pi)} \right)$	[3]
Piecewise Constant	$R_\infty + \frac{R_{ct}(\boldsymbol{\psi})}{\log\frac{\tau_1(\boldsymbol{\psi})}{\tau_0(\boldsymbol{\psi})}} \left(\log\left(1 - \frac{i}{2\pi f\tau_0(\boldsymbol{\psi})}\right) - \log\left(1 - \frac{i}{2\pi f\tau_1(\boldsymbol{\psi})}\right) \right)$	$\frac{R_{ct}(\boldsymbol{\psi})}{\log\frac{\tau_1(\boldsymbol{\psi})}{\tau_0(\boldsymbol{\psi})}} (H(\tau - \tau_0(\boldsymbol{\psi})) - H(\tau - \tau_1(\boldsymbol{\psi})))$	[24]
Fractal	$R_\infty + \frac{R_{ct}(\boldsymbol{\psi})}{(1 + i2\pi f\tau_0(\boldsymbol{\psi}))^\phi}$	$\begin{cases} \frac{R_{ct}(\boldsymbol{\psi})}{\pi} \sin(\phi\pi) \left(\frac{\tau}{\tau_0(\boldsymbol{\psi}) - \tau} \right)^\phi & \text{if } \tau < \tau_0 \\ 0 & \text{otherwise} \end{cases}$	[58]
LIB	$\left(\left(\left(\frac{1}{R_{ct}(T)} + (i2\pi fQ_e)^{\phi_1} \right)^{-1} + R_b(T) \right)^{-1} + (i2\pi fQ_g)^{\phi_2} \right)^{-1}$	$-\frac{1}{\pi} \left(Z'' \left(\frac{1}{2\pi} e^{-\log\tau + \frac{i\pi}{2}} \right) + Z'' \left(\frac{1}{2\pi} e^{-\log\tau - \frac{i\pi}{2}} \right) \right)$	[24, 59]

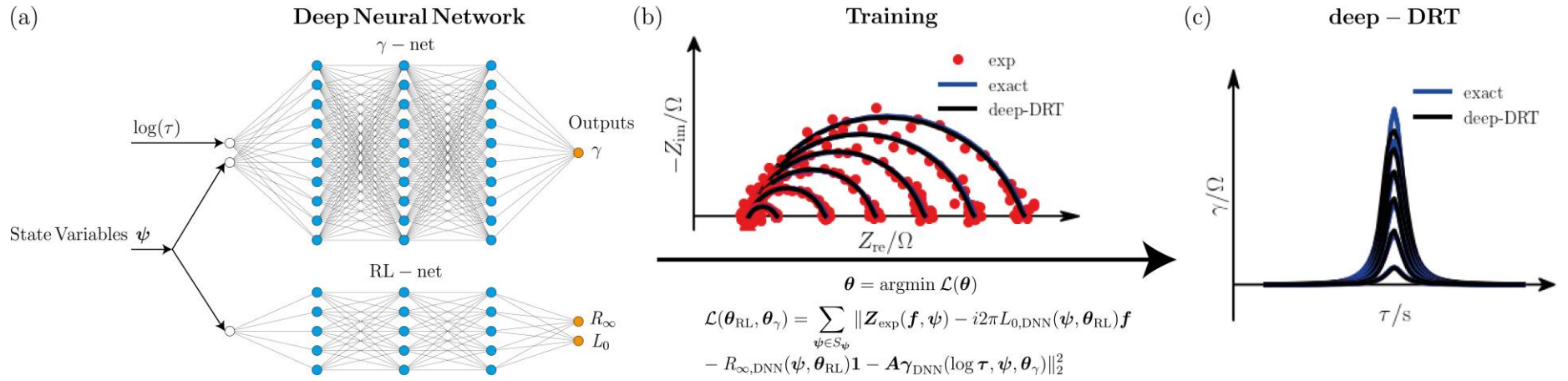


Figure 1 – Schematic depiction of the deep-DRT model. (a) The left portion depicts the γ - and RL- DNNs. The different colors of the DNNs' nodes indicate different activation functions (blue: ELU; orange: softplus). A timescale τ and parameters ψ are fed into the DNN. (b) Minimization of the loss with respect to the network parameters θ_γ and θ_{RL} is used to train the model (center image) and (c) estimate the DRT (right image).

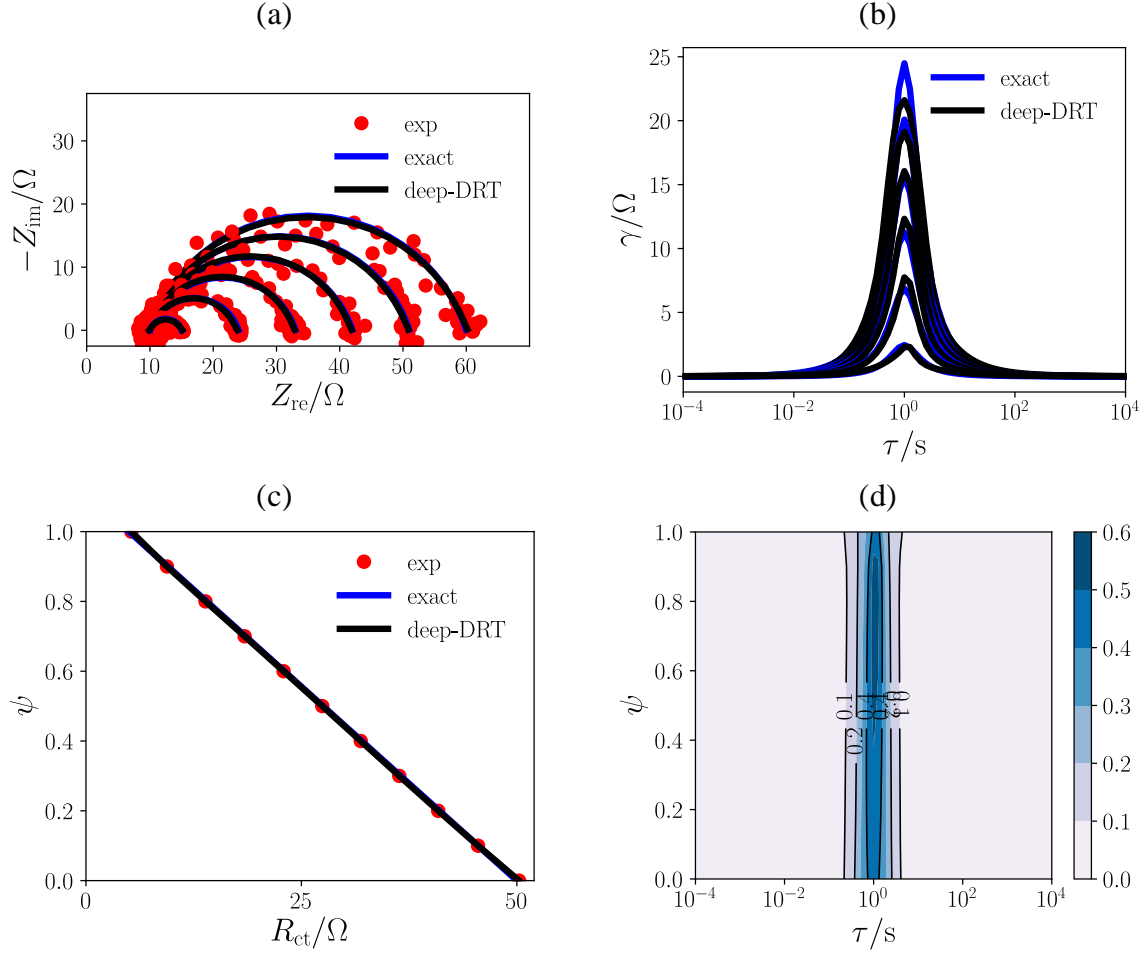


Figure 2 – Artificial impedance data generated using the ZARC model with $R_{\text{ct}}(\psi)$ linearly dependent on ψ . (a) Nyquist diagram of “experimental”, exact, and 2D deep-DRT impedances and (b) corresponding exact and recovered DRTs are shown for $\psi = 0, 0.2, \dots 1$. (c) $R_{\text{ct,DNN}}(\psi)$ and $R_{\text{ct,exact}}(\psi)$ as a function of ψ . Red dots correspond to the estimates $R_{\text{ct,DNN}}(\psi)$ ’s for $S_{\psi}^{\text{regress}} = S_{\psi}$ (regression dataset). (d) $\gamma_{\text{DNN,norm}}(\log \tau, \psi)$.

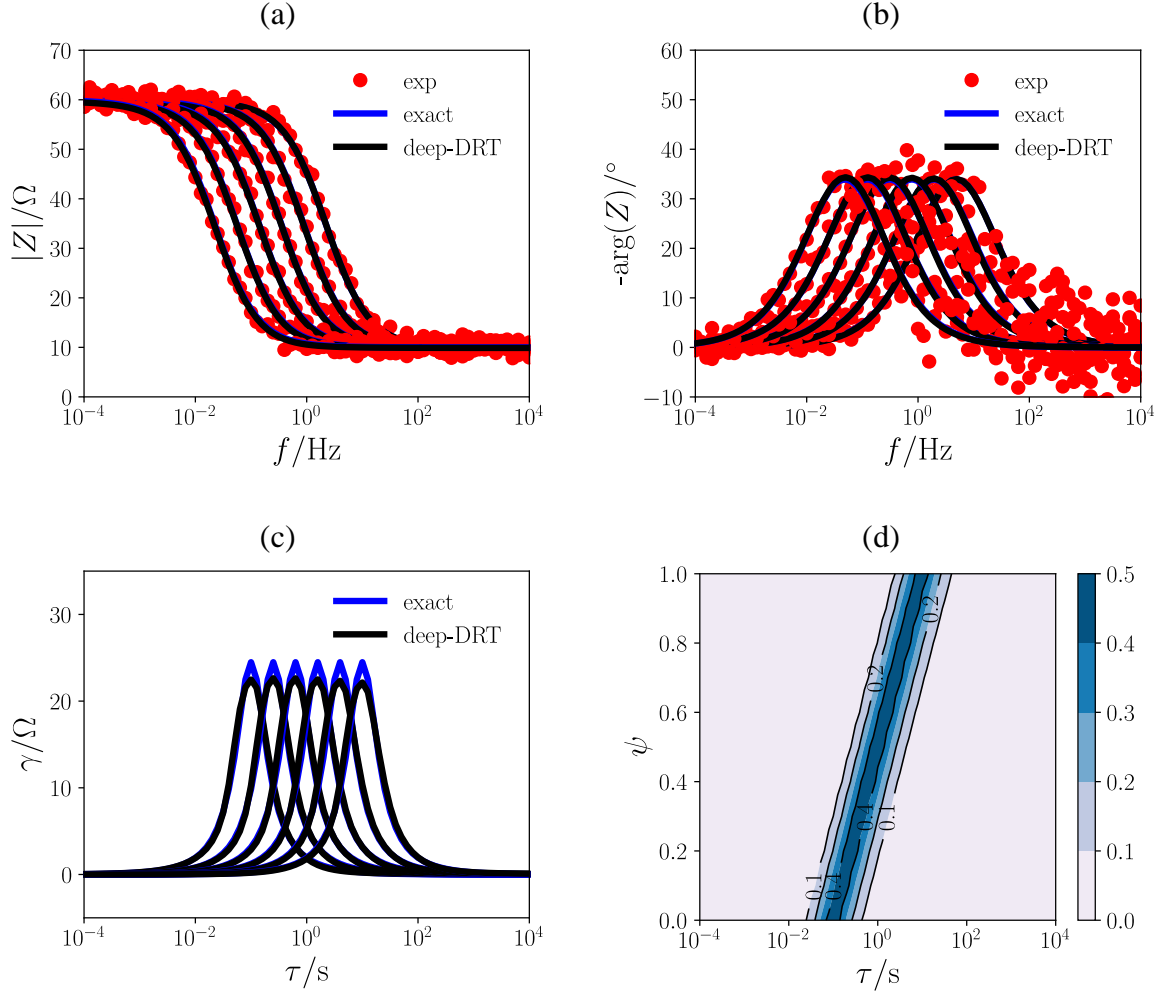


Figure 3 – Artificial impedance data generated using the ZARC model with $\tau_0(\psi)$ exponentially dependent on ψ . (a) Magnitude and (b) phase of “experimental”, exact, and 2D deep-DRT impedances are shown for $\psi = 0, 0.2, \dots 1$. (c) Exact and recovered DRTs, and (d) $\gamma_{\text{DNN,norm}}(\log \tau, \psi)$.

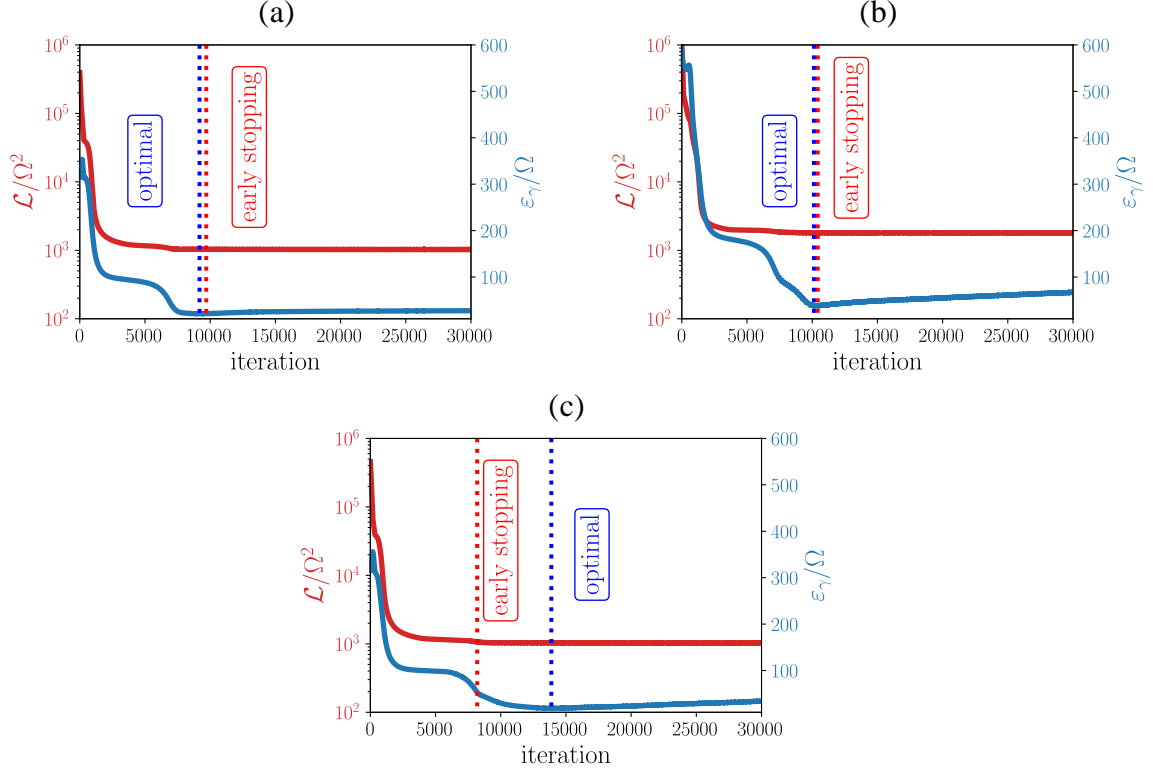


Figure 4 – Evolution of loss $\mathcal{L}(\boldsymbol{\theta}_{\text{RL}}, \boldsymbol{\theta}_\gamma)$ and error ε_γ as a function of iteration number with early stopping and optimal iterations shown. (a) $R_{\text{ct}}(\psi)$ linearly, (b) $\tau_0(\psi)$ exponentially, and (c) $R_{\text{ct}}(\psi)$ linearly and $\tau_0(\psi)$ exponentially dependent on ψ .

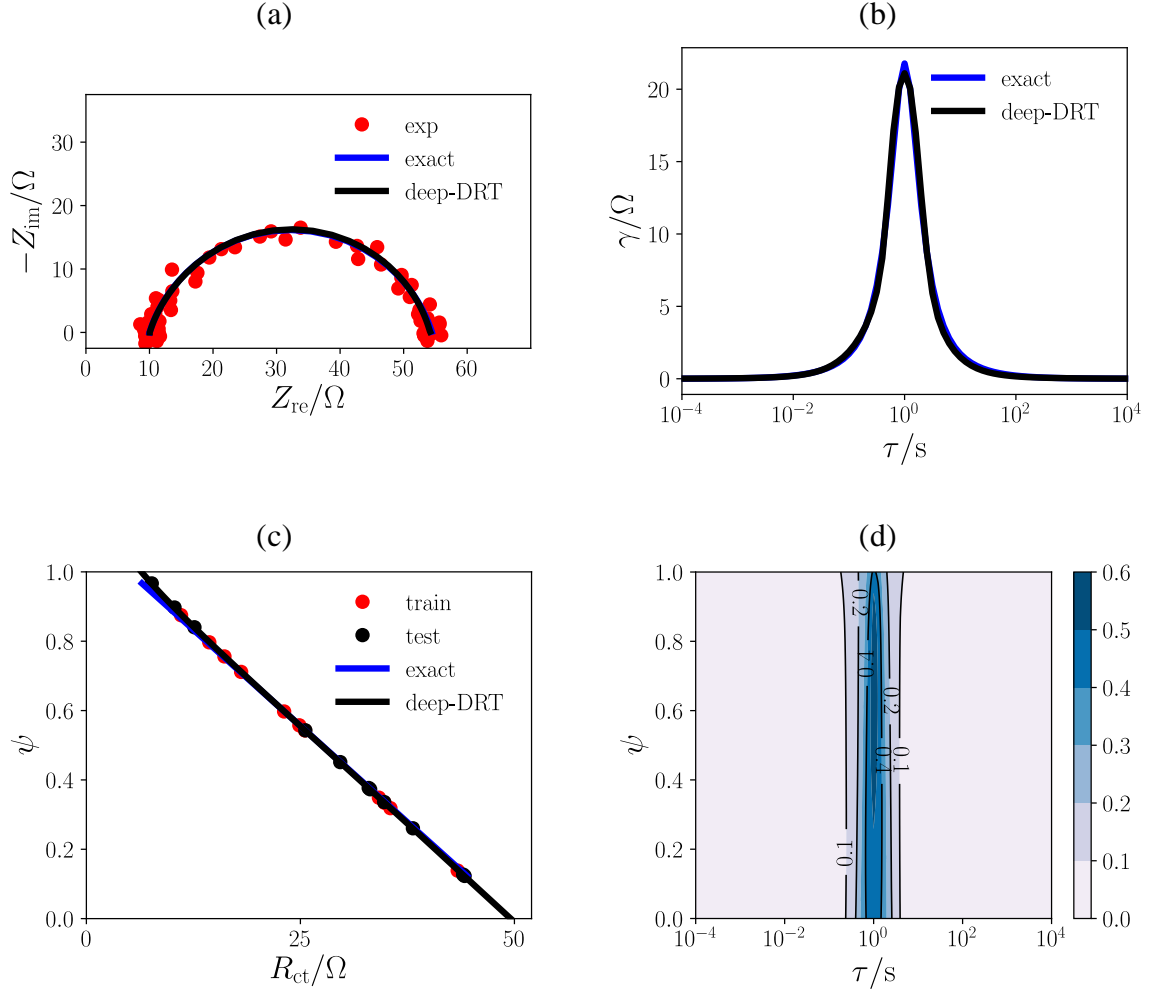


Figure 5 – Artificial impedance data generated using the ZARC model with $R_{\text{ct}}(\psi)$ linearly dependent on ψ . Note that the ψ was randomly sampled over $[0,1]$. (a) Nyquist diagram of “experimental”, exact, and 2D deep-DRT impedance. (b) Exact and recovered DRT are shown for $\psi = 0.12 \in S_{\psi}^{\text{test}}$ (test dataset) (c) $R_{\text{ct,DNN}}(\psi)$ and $R_{\text{ct,exact}}(\psi)$ as a function of ψ . Red and black dots correspond to the data used for training and test datasets, respectively. (d) $\gamma_{\text{DNN,norm}}(\log \tau, \psi)$.

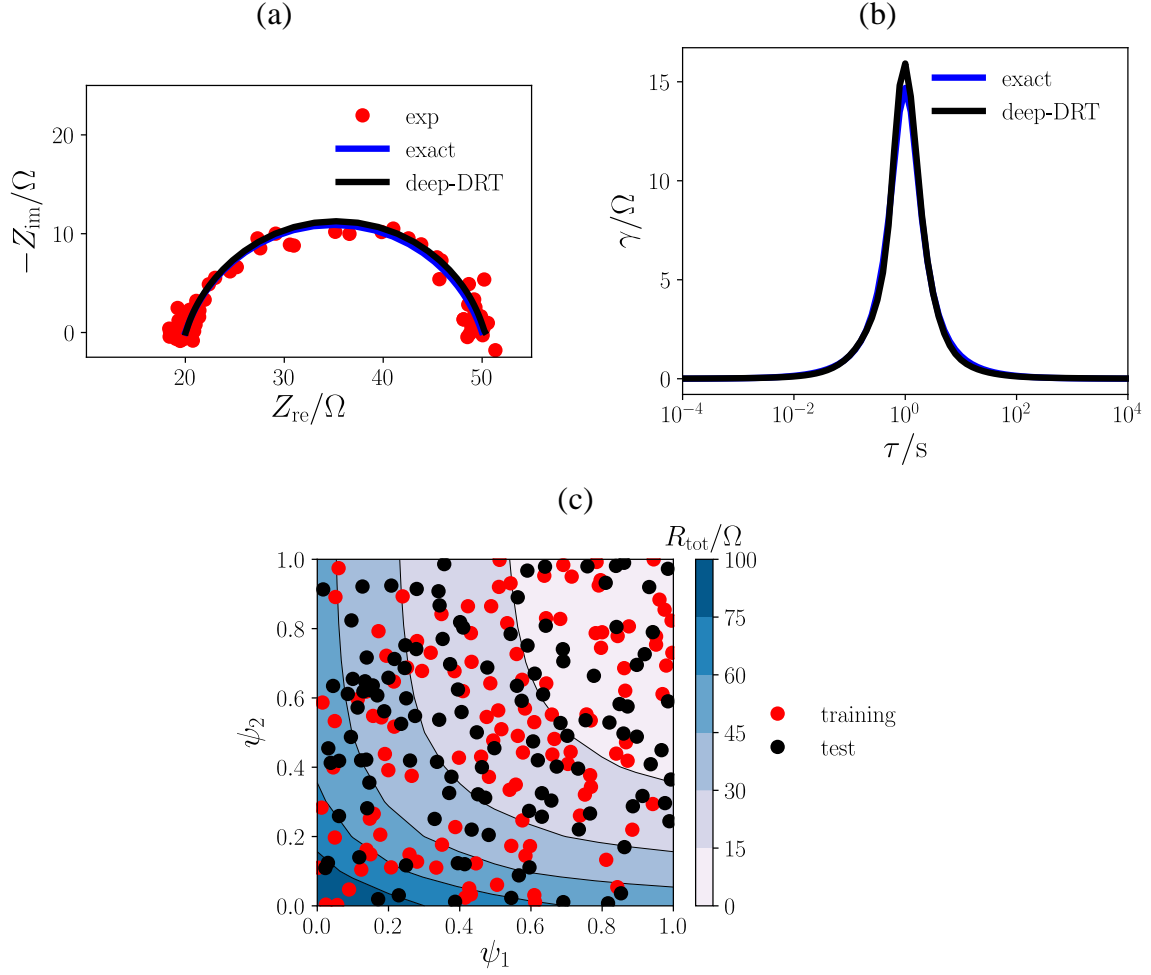


Figure 6 – Artificial impedance data generated using the ZARC model with $R_{\text{ct}}(\boldsymbol{\psi})$ exponentially dependent on $\boldsymbol{\psi} = [\psi_1, \psi_2]^\top$. Note that the $\boldsymbol{\psi}$ was randomly sampled over $[0,1] \times [0,1]$. (a) Nyquist diagram of “experimental”, exact, and 3D deep-DRT impedances. (b) Exact and recovered DRTs are shown for $\boldsymbol{\psi} = [0.38, 0.37] \in S_{\boldsymbol{\psi}}^{\text{test}}$ (test dataset). (c) $R_{\text{tot}}(\boldsymbol{\psi})$ shown as a contour plot as a function of $\boldsymbol{\psi}$ and estimates $R_{\text{tot,DNN}}(\boldsymbol{\psi})$ ’s, where red and black dots correspond to training $S_{\boldsymbol{\psi}}^{\text{train}}$ and test $S_{\boldsymbol{\psi}}^{\text{test}}$ datasets, respectively.

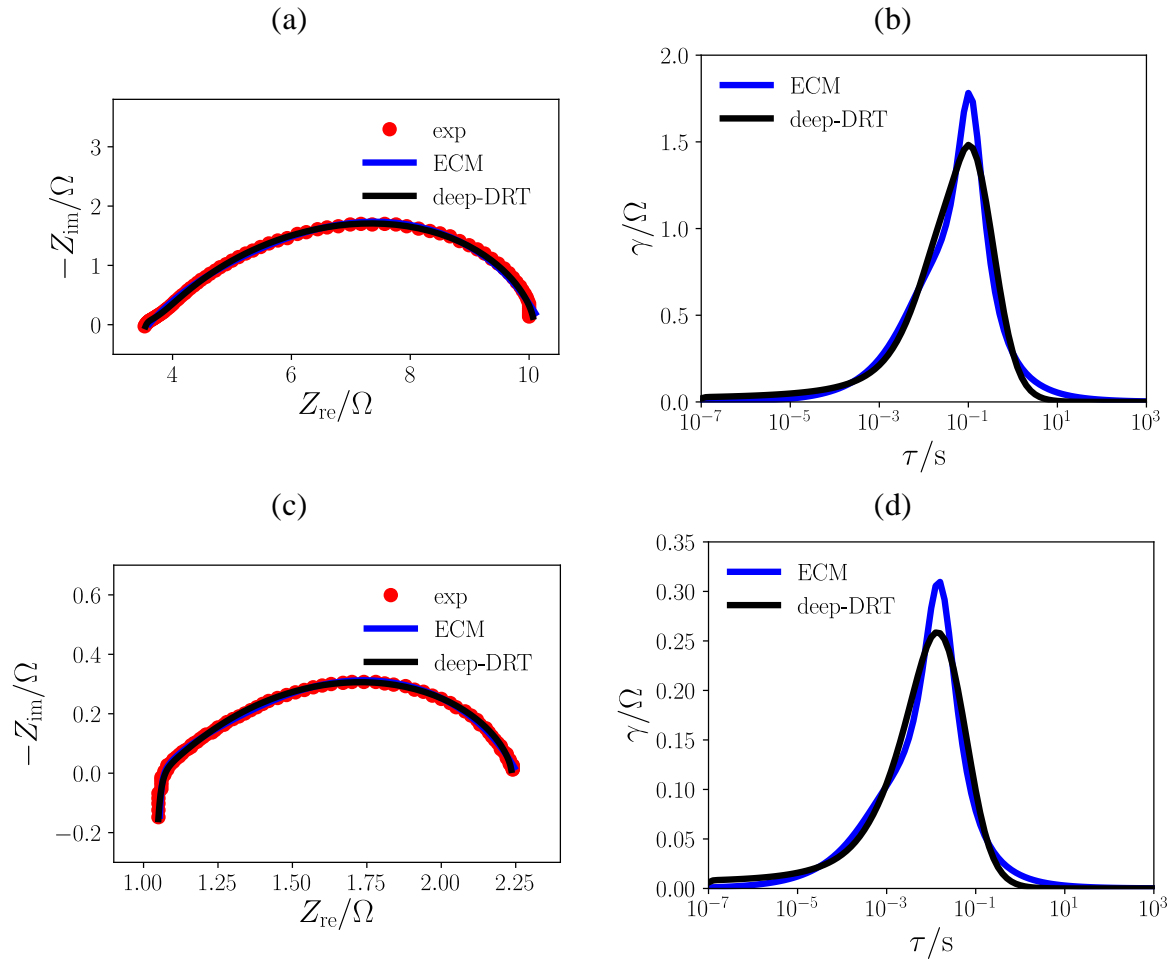


Figure 7 – Experimental EIS data from a symmetric cell with BLF-D5 at $p_{O_2} = 0.21$ atm. Nyquist diagrams of experimental, ECM, and 3D deep-DRT impedance, and corresponding recovered DRTs. (a) and (b) correspond to 500 °C and (c) and (d) to 600 °C.

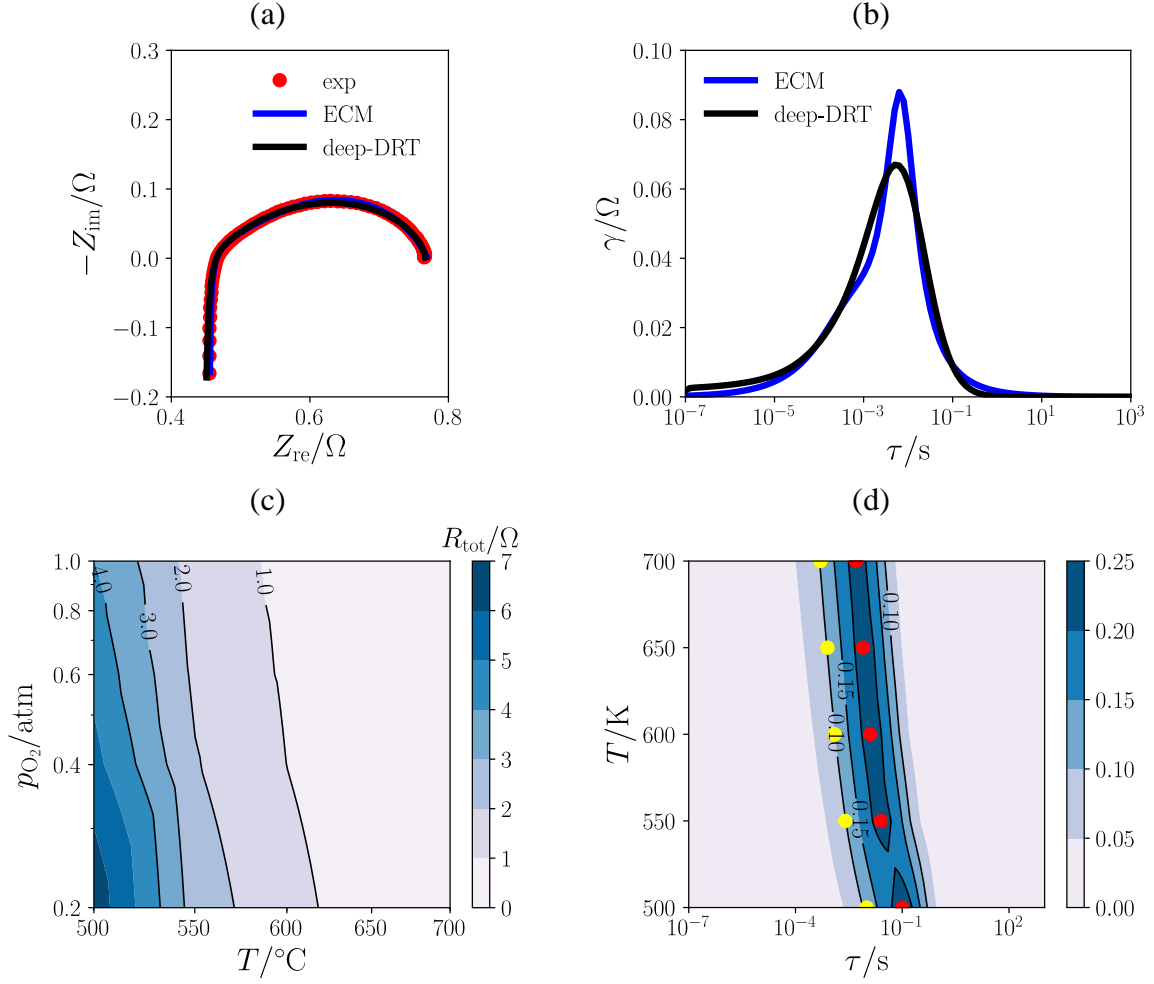


Figure 8 – Experimental EIS data from a symmetric cell with BLF-D5 at $p_{O_2} = 0.21$ atm and $T = 700$ °C. (a) Nyquist diagram of experimental, ECM, and 3D deep-DRT impedance, and (b) correspondingly recovered DRT. Contour plots of (c) $R_{tot}(T, p_{O_2})$ and (d) $\gamma_{norm,DNN}(\log \tau, T, p_{O_2})$. In panel (d), red and yellow dots show the DRT peak locations as obtained with the ECM.

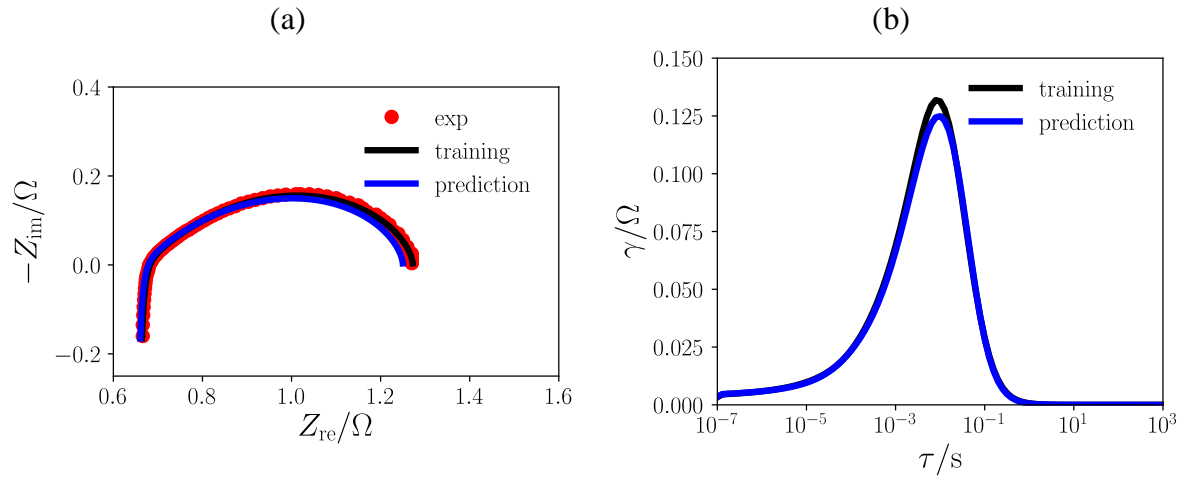


Figure 9 – Experimental EIS data from a symmetric cell with BLF-D5 at $T = 650$ °C, $p_{O_2} = 0.21$ atm. (a) Nyquist diagram of experimental, trained, and predicted 3D deep-DRT impedances and (b) correspondingly recovered DRTs. “Training” impedances and DRTs were obtained by regressing the full dataset. “Prediction” curves were obtained by the trained 3D deep-DRT model on the test dataset.

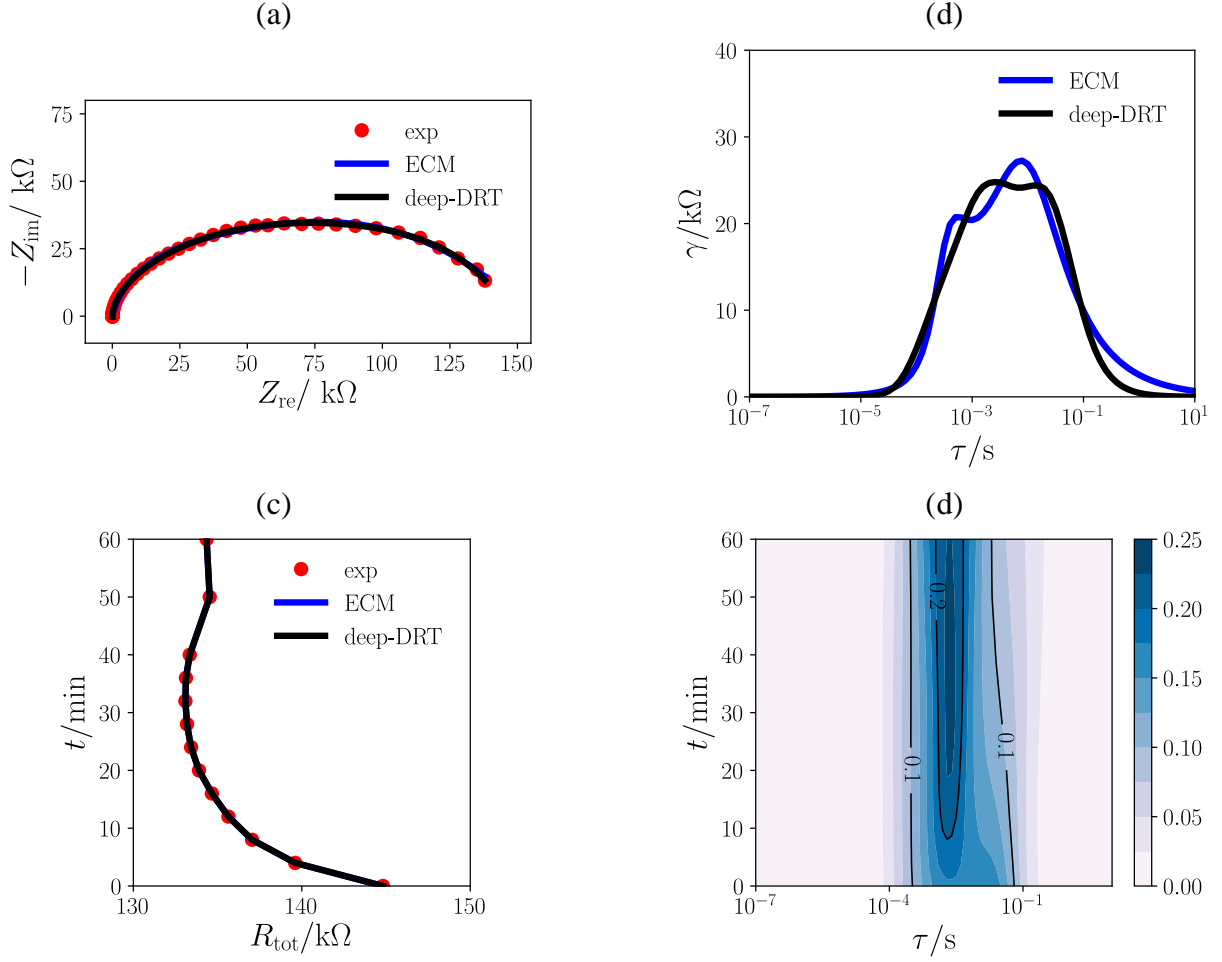


Figure 10 – Experimental EIS data from a perovskite solar cell, group 1 (from 1 atm of pure N_2 to 1 atm of pure O_2 ; from $t = 0$ to 60 mins). (a) Nyquist diagram of experimental, ECM, and 2D deep-DRT impedances with (b) corresponding ECM-based and 2D deep-DRTs at $t = 0$ min. (c) $R_{\text{tot,DNN}}(t)$ and $R_{\text{tot,ECM}}(t)$ as a function of t . Red dots correspond to the estimates $R_{\text{tot,DNN}}(t)$'s at the K_t experiments (regression dataset). (d) $\gamma_{\text{norm,DNN}}(\log \tau, t)$.

References:

- [1] D.D. Macdonald, Reflections on the history of electrochemical impedance spectroscopy, *Electrochimica Acta*, 51 (2006) 1376-1388.
- [2] A.J. Bard, L.R. Faulkner, *Electrochemical methods: fundamentals and applications*, Wiley New York 2001.
- [3] A. Lasia, *Electrochemical impedance spectroscopy and its applications*, Springer 2014.
- [4] V.F. Lvovich, *Impedance spectroscopy: applications to electrochemical and dielectric phenomena*, John Wiley & Sons 2012.
- [5] A. Nishikata, Y. Ichihara, T. Tsuru, An application of electrochemical impedance spectroscopy to atmospheric corrosion study, *Corrosion Science*, 37 (1995) 897-911.
- [6] Z. He, F. Mansfeld, Exploring the use of electrochemical impedance spectroscopy (EIS) in microbial fuel cell studies, *Energy & Environmental Science*, 2 (2009) 215-219.
- [7] A.-K. Hjelm, G. Lindbergh, Experimental and theoretical analysis of LiMn_2O_4 cathodes for use in rechargeable lithium batteries by electrochemical impedance spectroscopy (EIS), *Electrochimica Acta*, 47 (2002) 1747-1759.
- [8] F. Ciucci, Modeling electrochemical impedance spectroscopy, *Current Opinion in Electrochemistry*, 13 (2019) 132-139.
- [9] P.J. Denissen, S.J. Garcia, Reducing subjectivity in EIS interpretation of corrosion and corrosion inhibition processes by in-situ optical analysis, *Electrochimica Acta*, 293 (2019) 514-524.
- [10] T.S. Mathis, N. Kurra, X. Wang, D. Pinto, P. Simon, Y. Gogotsi, Energy storage data reporting in perspective—guidelines for interpreting the performance of electrochemical energy storage systems, *Advanced Energy Materials*, 9 (2019) 1902007.

- [11] M. Kissi, M. Bouklah, B. Hammouti, M. Benkaddour, Establishment of equivalent circuits from electrochemical impedance spectroscopy study of corrosion inhibition of steel by pyrazine in sulphuric acidic solution, *Applied Surface Science*, 252 (2006) 4190-4197.
- [12] M.E. Orazem, B. Tribollet, *Electrochemical impedance spectroscopy*, John Wiley & Sons 2017.
- [13] J. Liu, F. Ciucci, Modeling the impedance spectra of mixed conducting thin films with exposed and embedded current collectors, *Physical chemistry chemical physics : PCCP*, 19 (2017) 26310-26321.
- [14] F. Ciucci, T. Carraro, W.C. Chueh, W. Lai, Reducing error and measurement time in impedance spectroscopy using model based optimal experimental design, *Electrochimica Acta*, 56 (2011) 5416-5434.
- [15] F. La Mantia, J. Vetter, P. Novák, Impedance spectroscopy on porous materials: a general model and application to graphite electrodes of lithium-ion batteries, *Electrochimica Acta*, 53 (2008) 4109-4121.
- [16] D.A. Harrington, P. van den Driessche, Mechanism and equivalent circuits in electrochemical impedance spectroscopy, *Electrochimica Acta*, 56 (2011) 8005-8013.
- [17] J.R. Macdonald, Impedance spectroscopy: old problems and new developments, *Electrochimica Acta*, 35 (1990) 1483-1492.
- [18] S.C. Page, A.H. Anbuky, S.P. Krumdieck, J. Brouwer, Test method and equivalent circuit modeling of a PEM fuel cell in a passive state, *IEEE Transactions on Energy Conversion*, 22 (2007) 764-773.
- [19] A. Rodríguez, G.L. Plett, Controls-oriented models of lithium-ion cells having blend electrodes. Part 1: Equivalent circuits, *Journal of Energy Storage*, 11 (2017) 162-177.

- [20] F. Dion, A. Lasia, The use of regularization methods in the deconvolution of underlying distributions in electrochemical processes, *Journal of Electroanalytical Chemistry*, 475 (1999) 28-37.
- [21] E. Ivers-Tiffée, A. Weber, Evaluation of electrochemical impedance spectra by the distribution of relaxation times, *Journal of the Ceramic Society of Japan*, 125 (2017) 193-201.
- [22] S. Dierickx, A. Weber, E. Ivers-Tiffée, How the distribution of relaxation times enhances complex equivalent circuit models for fuel cells, *Electrochimica Acta*, 355 (2020) 136764.
- [23] J.G. Lyagaeva, G.K. Vdovin, D.A. Medvedev, Distinguishing bulk and grain boundary transport of a proton-conducting electrolyte by combining equivalent circuit scheme and distribution of relaxation times analyses, *The Journal of Physical Chemistry C*, 123 (2019) 21993-21997.
- [24] F. Ciucci, C. Chen, Analysis of electrochemical impedance spectroscopy data using the distribution of relaxation times: a Bayesian and hierarchical Bayesian approach, *Electrochimica Acta*, 167 (2015) 439-454.
- [25] V.V. Lopes, C.M. Rangel, A.Q. Novais, Modelling and identification of the dominant phenomena in hydrogen fuel-cells by the application of DRT Analysis, *Computer Aided Chemical Engineering*, Elsevier 2013, pp. 283-288.
- [26] M. Saccoccio, T.H. Wan, C. Chen, F. Ciucci, Optimal regularization in distribution of relaxation times applied to electrochemical impedance spectroscopy: ridge and lasso regression methods - a theoretical and experimental study, *Electrochimica Acta*, 147 (2014) 470-482.
- [27] T.H. Wan, M. Saccoccio, C. Chen, F. Ciucci, Influence of the discretization methods on the distribution of relaxation times deconvolution: implementing radial basis functions with DRTtools, *Electrochimica Acta*, 184 (2015) 483-499.
- [28] J. Kaipio, E. Somersalo, Statistical inverse problems: discretization, model reduction and inverse crimes, *Journal of Computational and Applied Mathematics*, 198 (2007) 493-504.

- [29] D. Calvetti, E. Somersalo, Inverse problems: from regularization to Bayesian inference, *WIREs Computational Statistics*, 10 (2018) e1427.
- [30] J. Huang, M. Papac, R. O'Hayre, Towards robust autonomous impedance spectroscopy analysis: A calibrated hierarchical Bayesian approach for electrochemical impedance spectroscopy (EIS) inversion, *Electrochimica Acta*, 367 (2021) 137493.
- [31] A.N. Tikhonov, A. Goncharsky, V. Stepanov, A.G. Yagola, Numerical methods for the solution of ill-posed problems, Springer Science & Business Media 2013.
- [32] A. Mikonis, J. Banys, R. Grigalaitis, A. Matulis, S. Lapinskas, G. Völkel, Determination of the two dimensional distribution of the attempt relaxation times and activation energies from temperature dependence of dielectric dispersion, *Open Physics*, 11 (2013) 206-212.
- [33] R.A. Renaut, R. Baker, M. Horst, C. Johnson, D. Nasir, Stability and error analysis of the polarization estimation inverse problem for microbial fuel cells, *Inverse Problems*, 29 (2013) 045006.
- [34] X. Li, M. Ahmadi, L. Collins, S.V. Kalinin, Deconvolving distribution of relaxation times, resistances and inductance from electrochemical impedance spectroscopy via statistical model selection: exploiting structural-sparsity regularization and data-driven parameter tuning, *Electrochimica Acta*, 313 (2019) 570-583.
- [35] J.R. Macdonald, Comparison of parametric and nonparametric methods for the analysis and inversion of immittance data: critique of earlier work, *Journal of Computational Physics*, 157 (2000) 280-301.
- [36] E. Tuncer, S. Gubanski, On dielectric data analysis. Using the Monte Carlo method to obtain relaxation time distribution and comparing non-linear spectral function fits, *IEEE Transactions on Dielectrics and Electrical Insulation*, 8 (2001) 310-320.

- [37] S. Hershkovitz, S. Baltianski, Y. Tsur, Harnessing evolutionary programming for impedance spectroscopy analysis: a case study of mixed ionic-electronic conductors, *Solid State Ionics*, 188 (2011) 104-109.
- [38] S. Hershkovitz, S. Baltianski, Y. Tsur, Electrochemical impedance analysis of SOFC cathode reaction using evolutionary programming, *Fuel Cells*, 12 (2012) 77-85.
- [39] A.K. Baral, Y. Tsur, Impedance spectroscopy of Gd-doped ceria analyzed by genetic programming (ISGP) method, *Solid State Ionics*, 304 (2017) 145-149.
- [40] T. Hörlin, Maximum entropy in impedance spectroscopy of non-inductive systems, *Solid State Ionics*, 67 (1993) 85-96.
- [41] T. Hörlin, Deconvolution and maximum entropy in impedance spectroscopy of noninductive systems, *Solid State Ionics*, 107 (1998) 241-253.
- [42] B.A. Boukamp, Fourier transform distribution function of relaxation times; application and limitations, *Electrochimica Acta*, 154 (2015) 35-46.
- [43] S. Effendy, J. Song, M.Z. Bazant, Analysis, design, and generalization of electrochemical impedance spectroscopy (EIS) inversion algorithms, *Journal of The Electrochemical Society*, 167 (2020) 106508.
- [44] M.B. Effat, F. Ciucci, Bayesian and hierarchical bayesian based regularization for deconvolving the distribution of relaxation times from electrochemical impedance spectroscopy data, *Electrochimica Acta*, 247 (2017) 1117-1129.
- [45] J. Liu, F. Ciucci, The Gaussian process distribution of relaxation times: a machine learning tool for the analysis and prediction of electrochemical impedance spectroscopy data, *Electrochimica Acta*, 331 (2020) 135316.
- [46] J. Liu, F. Ciucci, The Deep-prior distribution of relaxation times, *Journal of The Electrochemical Society*, 167 (2020) 026506.

- [47] R. O'Hayre, S.W. Cha, W. Colella, F.B. Prinz, Fuel cell fundamentals, John Wiley & Sons 2016.
- [48] H. Sumi, H. Shimada, Y. Yamaguchi, T. Yamaguchi, Y. Fujishiro, Degradation evaluation by distribution of relaxation times analysis for microtubular solid oxide fuel cells, *Electrochimica Acta*, 339 (2020) 135913.
- [49] B.A. Boukamp, A. Rolle, Use of a distribution function of relaxation times (DFRT) in impedance analysis of SOFC electrodes, *Solid State Ionics*, 314 (2018) 103-111.
- [50] A. Mertens, J. Granwehr, Two-dimensional impedance data analysis by the distribution of relaxation times, *Journal of Energy Storage*, 13 (2017) 401-408.
- [51] A. Belotti, J. Liu, A. Curcio, Y. Wang, S. Pepe, E. Quattrocchi, F. Ciucci, Influence of A-site deficiency on the electrochemical performance of the cobalt-free cathode $(\text{Ba}_{0.95}\text{La}_{0.05})_{1-x}\text{FeO}_{3-\delta}$, (In preparation).
- [52] I. Zarazua, G. Han, P.P. Boix, S. Mhaisalkar, F. Fabregat-Santiago, I. Mora-Sero, J. Bisquert, G. Garcia-Belmonte, Surface Recombination and Collection Efficiency in Perovskite Solar Cells from Impedance Analysis, *The journal of physical chemistry letters*, 7 (2016) 5105-5113.
- [53] W. Ni, T. Zhu, X. Chen, Q. Zhong, W. Ma, Stable, efficient and cost-competitive Ni-substituted $\text{Sr}(\text{Ti},\text{Fe})\text{O}_3$ cathode for solid oxide fuel cell: Effect of A-site deficiency, *Journal of Power Sources*, 451 (2020) 227762.
- [54] D.-A. Clevert, T. Unterthiner, S. Hochreiter, Fast and accurate deep network learning by exponential linear units (ELUs), *arXiv preprint arXiv:1511.07289*, (2015).
- [55] D.P. Kingma, J.L. Ba, Adam: A method for stochastic optimization, *arXiv preprint arXiv:1412.6980*, (2014).
- [56] G.B. Orr, K.-R. Müller, Neural networks: tricks of the trade, Springer 1998.

- [57] A. Paszke, S. Gross, S. Chintala, G. Chanan, E. Yang, Z. DeVito, Z. Lin, A. Desmaison, L. Antiga, A. Lerer, Automatic differentiation in Pytorch, 31st Conference on Neural Information Processing Systems (NIPS 2017) Long Beach, CA, USA., 2017.
- [58] E. Barsoukov, Impedance spectroscopy: theory, experiment, and applications, John Wiley 2017.
- [59] M. Watanabe, K. Sanui, N. Ogata, F. Inoue, T. Kobayashi, Z. Ohtaki, Temperature dependence of ionic conductivity of crosslinked poly (propylene oxide) films dissolving lithium salts and their interfacial charge transfer resistance in contact with lithium electrodes, *Polymer Journal*, 16 (1984) 711-716.
- [60] R.M. Fuoss, J.G. Kirkwood, Electrical properties of solids. VIII. Dipole moments in polyvinyl chloride-diphenyl systems, *Journal of the American Chemical Society*, 63 (1941) 385-394.
- [61] A. Belotti, J. Liu, A. Curcio, Y. Wang, S. Pepe, E. Quattrocchi, F. Ciucci, Electrochemical performance of A-site deficient and La-stabilized $\text{Ba}_{0.95}\text{La}_{0.05}\text{FeO}_{3-\delta}$, (in preparation).
- [62] A. Jun, J. Kim, J. Shin, G. Kim, Perovskite as a cathode material: a review of its role in solid-oxide fuel cell technology, *ChemElectroChem*, 3 (2016) 511-530.
- [63] C. Kim, J. Kim, J. Shin, G. Kim, Effects of composite cathode on electrochemical and redox properties for intermediate-temperature solid oxide fuel cells, *International Journal of Hydrogen Energy*, 39 (2014) 20812-20818.
- [64] D. Kim, E.S. Muckley, N. Creange, T.H. Wan, M.H. Ann, E. Quattrocchi, R.K. Vasudevan, J.H. Kim, F. Ciucci, I.N. Ivanov, S.V. Kalinin, M. Ahmadi, Exploring transport behavior in hybrid perovskites solar cells via machine learning analysis of environmental-dependent impedance spectroscopy, submitted, (2020).